



**HAL**  
open science

## Satellite remote sensing estimation of river discharge: Application to the Yukon River Alaska

David M. Bjerklie, Charon M. Birkett, John W. Jones, Claudia Carabajal,  
Jennifer A. Rover, John W. Fulton, Pierre-André Garambois

### ► To cite this version:

David M. Bjerklie, Charon M. Birkett, John W. Jones, Claudia Carabajal, Jennifer A. Rover, et al..  
Satellite remote sensing estimation of river discharge: Application to the Yukon River Alaska. *Journal  
of Hydrology*, 2018, 561, pp.1000-1018. 10.1016/j.jhydrol.2018.04.005 . hal-02362515

**HAL Id: hal-02362515**

**<https://hal.science/hal-02362515v1>**

Submitted on 13 Nov 2019

**HAL** is a multi-disciplinary open access archive for the deposit and dissemination of scientific research documents, whether they are published or not. The documents may come from teaching and research institutions in France or abroad, or from public or private research centers.

L'archive ouverte pluridisciplinaire **HAL**, est destinée au dépôt et à la diffusion de documents scientifiques de niveau recherche, publiés ou non, émanant des établissements d'enseignement et de recherche français ou étrangers, des laboratoires publics ou privés.

# Accepted Manuscript

Research papers

Satellite Remote Sensing Estimation of River Discharge: Application to the Yukon River Alaska

David M. Bjerklie, Charon M. Birkett, John W. Jones, Claudia Carabajal, Jennifer A. Rover, John W. Fulton, Pierre-André Garambois

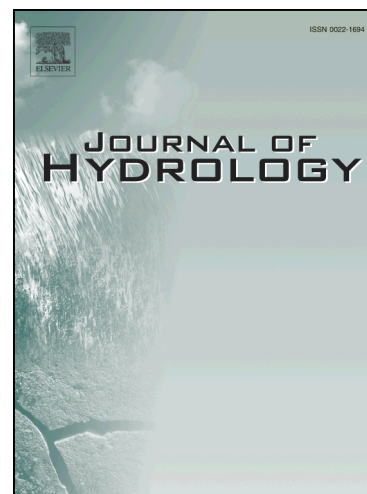
PII: S0022-1694(18)30246-4  
DOI: <https://doi.org/10.1016/j.jhydrol.2018.04.005>  
Reference: HYDROL 22708

To appear in: *Journal of Hydrology*

Received Date: 2 March 2017  
Revised Date: 16 February 2018  
Accepted Date: 1 April 2018

Please cite this article as: Bjerklie, D.M., Birkett, C.M., Jones, J.W., Carabajal, C., Rover, J.A., Fulton, J.W., Garambois, P-A., Satellite Remote Sensing Estimation of River Discharge: Application to the Yukon River Alaska, *Journal of Hydrology* (2018), doi: <https://doi.org/10.1016/j.jhydrol.2018.04.005>

This is a PDF file of an unedited manuscript that has been accepted for publication. As a service to our customers we are providing this early version of the manuscript. The manuscript will undergo copyediting, typesetting, and review of the resulting proof before it is published in its final form. Please note that during the production process errors may be discovered which could affect the content, and all legal disclaimers that apply to the journal pertain.



## Satellite Remote Sensing Estimation of River Discharge: Application to the Yukon River Alaska

David M. Bjerklie<sup>1</sup>, Charon M. Birkett<sup>2</sup>, John W. Jones<sup>3</sup>, Claudia Carabajal<sup>4</sup>, Jennifer A. Rover<sup>5</sup>,  
John W. Fulton<sup>1</sup>, Pierre-André Garambois<sup>6</sup>

1 – U.S. Geological Survey, Water Mission Area

2 – University of Maryland, ESSIC, College Park, MD

3 – U. S. Geological Survey, Eastern Geographic Science Center, 12201 Sunrise Valley Dr., Reston, VA.

4 - Sigma Space Corp. at NASA/GSFC, Greenbelt, Maryland

5 – U.S. Geological Survey EROS Science Center, Sioux Falls, SD

6 – ICUBE - UMR 7357, Fluid Mechanics Team, INSA Strasbourg, 24 Boulevard de la victoire, 67084 Strasbourg cedex, France

### ABSTRACT

A methodology based on general hydraulic relations for rivers has been developed to estimate the discharge (flow rate) of rivers using satellite remote sensing observations. The estimates of discharge, flow depth, and flow velocity are derived from remotely observed water surface area, water surface slope, and water surface height, and demonstrated for two reaches of the Yukon River in Alaska, at Eagle (reach length 34.7 km) and near Stevens Village (reach length 38.3 km). The method is based on fundamental equations of hydraulic flow resistance in rivers, including the Manning equation and the Prandtl-von Karman universal velocity distribution equation. The method employs some new hydraulic relations to help define flow resistance and height of the zero flow boundary in the channel. Estimates are made both with and without calibration. The water surface area of the river reach is measured by using a provisional version of the U.S. Geological Survey (USGS) Landsat based product named Dynamic Surface Water Extent (DSWE). The water surface height and slope measurements require a self-consistent datum, and are derived from observations from the Jason-2 satellite altimeter mission. At both reach locations, the Jason-2 radar altimeter non-winter heights consistently tracked the stage recorded at USGS streamgages with a standard deviation of differences (error) during the non-winter periods of less than 7%. Part of the error may be due to differences in the gage and altimeter crossing locations with respect to the range of stage change and the response to changes in discharge at the upstream and downstream locations. For the

non-winter periods, the radar derived slope estimates (mean=0.0003) were constant over the mission lifetime, and in agreement with previously measured USGS water surface slopes and slopes determined from USGS topographic maps. The accuracy of the mean of the uncalibrated daily estimates of discharge varied between reaches, ranging from 13% near Stevens Village (N=90) to -21% at Eagle (N = 246) based on the absolute error, and 5% to -6% based on the error of the log of the estimates. Calibrating to the mean of USGS daily discharge estimates from the streamflow rating for the same period of record at each streamgage resulted in mean absolute errors ranging from 1% to 2%, and log errors ranging from 1% or less. The error pattern of the estimates shows that without calibration, even though the mean is well simulated, the high and low end values over the range of estimates may have significant bias.

## 1.0 Introduction

Monitoring the hydrologic cycle is critical to the management of water resources as it is necessary to understand variations in the hydrologic cycle resulting from changes in climate, land use, and water use (Vörösmarty et al., 2000). Evaluating the accuracy of the net atmospheric exchange of water over land is fully dependent on understanding the change in land surface storage of water and the transport of water to the oceans from rivers (Fekete and Vörösmarty, 2007). Knowledge of river flow (discharge) as well as lake and wetland storage volume is also important for examining mass water balance across inland water basins. However, in many parts of the globe, dense monitoring networks of land surface hydrologic fluxes are not available as collected gage information may be restricted, or lakes and rivers may be so remote or inaccessible that gage deployment and maintenance are prohibitive. Given these challenges, coverage by existing networks is declining (Shiklomanov et al., 2002; Fekete and Vörösmarty, 2007). Thus, satellite based monitoring of surface storage change and river discharge has been an ongoing goal of the remote sensing community (Alsdorf et al., 2003). Of particular interest to global hydrology is remote sensing of surface water dynamics in high northern latitudes because of the difficulty and expense of access and the sensitivity of this region to change in climate (Carroll et al., 2016).

Because of potential climate change effects on water quality, availability, and hydrology, the Yukon River basin is a major focus region for the USGS with on-going studies that are setting the baseline for future changes within the river and its major tributaries. These programs are particularly examining the processes that affect or control water quality and availability. With climate change potentially causing permafrost regions to melt, the soil can be transformed into biogeochemically active zones altering both water quality and discharge. Recent studies have shown that total carbon yield can be directly proportional to discharge (Walvoord and Striegl, 2007). Thus changes in discharge may affect carbon transport in Alaska. Multi-decadal trends in the areal extent of wetlands and lakes in central Alaska indicate that ~85% of these water bodies have not experienced significant change (Rover et al., 2012), although these trends may not persist. The long-term collection and availability of high quality water resources data are crucial to understanding the relations and sensitivities among climate, water resources, and the health of ecosystems. Yet only three USGS streamgages exist on the Yukon River main stem in Alaska. This river basin is therefore an important place to develop synergistic use of satellite altimetry and imagery for the estimation of discharge.

Remotely sensed measurements could enhance the ground-based networks. For example, recent research studies have highlighted the potential of the German TerraSAR-X InSAR (SAR, synthetic aperture radar) instrument for estimating line-of-sight surface currents (Romeiser et al., 2005) and the potential of the wide-swath radar imaging for water surface elevation mapping (Kim et al., 2014; Alsdorf et al., 2007). Currently, no satellite-based system has the ability to measure river discharge directly. However the utilization of remotely sensed hydraulic parameters such as water-surface width, slope, and elevation has been explored with a view to obtaining channel discharge (Smith et al., 1996; Smith, 1997; Bjerklie et al., 2003 and 2005; Dingman and Bjerklie, 2006; Brakenridge et al., 2007; LeFavour and Alsdorf, 2005; Leon et al., 2006; and Bjerklie, 2007). While various optical, near-infrared, passive and active microwave imaging sensors form the basis for determining surface extent or width, interferometric SAR (e.g. Alsdorf

et al., 2001) and radar and laser altimetry have come to the forefront for their ability to determine water-surface elevation.

Recent efforts have been underway to evaluate the application of various algorithms to estimate discharge in rivers from remote observations of the river channel (Bonnema et al., 2016; Durand et al., 2016) in support of the upcoming NASA Surface Water and Ocean Topography (SWOT) mission (<http://swot.jpl.nasa.gov/mission/>). Scheduled to launch in 2021, SWOT is designed to make the first global survey of Earth's surface water. Key to this effort is the inclusion of a wide swath radar that is expected to provide water surface extent, height, and slope in rivers of 100 m or greater width.

Previous work has demonstrated the efficacy of using Landsat imagery to track surface water dynamics and develop time series of water surface change in diverse regions of the world (Carroll et al., 2016; Jones, 2015; Kim et al., 2014; Tulbure and Broich, 2013). Additionally, satellite based radar altimeters have been used to track river dynamics (Birkett, 1998, Birkett et al., 2002) and to develop discharge rating curves (relating stage and discharge) for large rivers given ground-based measurements of discharge (Kouraev 2004; Papa et al., 2012) or discharge estimated from hydrodynamic models (Paiva et al., 2013; Leon et al., 2006; Getirana and Peters-Lidard, 2013; Getirana et al., 2009; Paris et al., 2016). Rating curves have also been developed in braided river systems by using remotely sensed river width and ground-based discharge (Smith et al., 1996; Pavelsky, 2014). Brakenridge et al. (2007) has shown that discharge ratings can also be developed from the reflectance properties of microwave radiation, which is sensitive to water content within a pixel, in correlation with the ground-measured river discharge.

Other research has focused specifically on developing discharge estimation algorithms that will use observations from the SWOT mission or other satellites independent from ground-based discharge measurements. These algorithms use one or more of the satellite observed water surface width (surface

area), slope, and/or height as input variables. For example, Gleason and Smith (2014) have shown that observations of width alone, in the context of reach scale hydraulic geometry, can be used to estimate discharge in a number of rivers with less than 30% root mean squared error (RMSE). Birkinshaw et al. (2010; 2014) demonstrated that satellite derived stage, slope, and width can be used to estimate discharge between gaged locations by using the gage discharge as a boundary condition or using limited discharge information to derive a suitable reference depth. Durand et al. (2014) used inverse modeling techniques to estimate discharge in the River Severn, United Kingdom, using a physically based flow resistance equation using initial estimates of the unknown parameters, including bottom depth and a flow resistance coefficient. Similarly, Garambois and Monnier (2015) used inverse methods and remote observations of river surface features to estimate various hydraulic properties of the river flow in the Garonne River, France/Spain. Both methods produced estimates within 15% of observed discharge. Durand et al. (2016) and Bonnema et al. (2016) used modeled river data as a proxy for the future SWOT observations to test various physically based and quasi physically based discharge algorithms in a set of rivers in the U.S. and France, and in the Ganges-Brahmaputra, India. They used modeled water surface area of the river to provide a reach average width, and the height (stage) for the water surface along the reach to provide surface slope as an index to change in flow depth. The discharge algorithms tested in Durand et al. (2016) and Bonnema et al. (2016) vary in accuracy depending on river and reach, and the results may be quite good in some cases (within 10% RMSE).

This paper introduces and tests a revised methodology for river discharge estimation based on satellite-derived hydraulic variables. Satellite sensing technologies include publicly available, systematically collected optical imaging as well as laser and radar altimetry. The optical data (described in section 2.6) are used to estimate reach mean flow width under various flow conditions. The laser and radar altimetry data are both employed for surface water height and river reach slope estimation. The study basin is the Yukon River with a focus on two specific reaches where USGS in-situ data are available: the Yukon River streamgages above Eagle and Stevens Village.

## 2.0 Methods

Our approach links remotely sensed variables to those used in standard discharge equations through relationships derived from USGS in situ observations. This section briefly describes the study area in situ data, summarizes the derivation of hydraulic relations to link remotely sensed observations to discharge equations, and provides an overview of the satellite-derived data used.

### 2.1 Study Area Streamflow and Stage Data

The Yukon River flows from the fourth largest river basin in North America and is one of the largest rivers flowing from the Arctic Region (Brabets et al., 1999) with a drainage area of  $\sim 855,000$  km<sup>2</sup> and an average flow of 6,430 cubic meters per second (m<sup>3</sup>/s). The Yukon River main stem and most of its major tributaries begin as high-gradient rivers draining the rugged mountain ranges in northern British Columbia. Ground-measured streamflow and stage data were obtained from the USGS National Water Information System (NWIS) website for two streamgages on the Yukon, the gage at Eagle, Alaska (station number 15356000; drainage area 111,600 square miles, latitude 64° 46'22", longitude 141°11'52" NAD27) and the gage near Stevens Village, Alaska (station number 15453500; drainage area 194,000 square miles, latitude 65° 52'32", longitude 149°43'04" NAD27). Stage (water surface height) is measured and recorded every fifteen minutes during ice-free conditions and is available on the NWIS website in real time. We compiled from the USGS NWIS data base the daily mean values of stage for the period of record coinciding with the Jason-2 altimeter observations (see the online read\_me and metadata at <ftp://ftp.nodc.noaa.gov/pub/data.nodc/jason2/>) used in this study (July 2008 to October 2016). The stage measurements are referenced to an elevation datum that is maintained near each gage, NAVD 1988 near Stevens Village, and NGVD 1929 at Eagle. The USGS does not measure slope at either of these gages.



Additionally, during regular site visits to each streamgage, acoustic Doppler current profilers (ADCP) measured the water surface width, depth, and velocity at a cross-section in proximity to the stage recorders. In practice, such measurements are made a number of times each year, and these values are then correlated in a one-to-one relation with the stage value at the time of the measurement. These paired values create the stage-discharge rating that is used to derive the estimates of real-time discharge. For this study, we used the published daily mean values of stage and discharge from NWIS.

Based on measurements from the streamgage data, the ice-free in-bank width and stage of the Yukon River vary depending on flow. Width varies roughly from 330 to 500 m at Eagle and 600 to nearly 800 m at Stevens Village. Stage varies up to 4 m at Eagle and up to 9 m at Stevens Village. The river typically freezes over completely during much of the winter months (October through April), although climate conditions are becoming less predictable in the Yukon River Basin (Brabets et al., 1999). During the winter, river flow typically declines, and the ice surface may be intermittently snow covered, indicating that the stage and slope of the river surface during these periods would not reflect the water surface because of the ice and snow accumulation. During the open-water period (May through October) the water surface slope may vary over an unknown range.

## 2.2 Development of Hydraulic Relations

We compare the effectiveness of two generally accepted one-dimensional flow resistance equations: the familiar Manning equation (MAN) (eq. 1); and a theoretically based equation developed from the Prandtl-von Karman (PVK) (eq. 2) universal velocity distribution (Dingman, 2009; Chow, 1959). The key challenge in applying these equations is the estimation of a flow resistance term and the flow depth from the observed hydraulic variables. We explored several general hydraulic variables to estimate these unknowns. The depth of the river used by MAN and PVK is derived from stage and width observations

coupled with geometric assumptions regarding the channel cross-section shape. The data requirements and sources of information for applying the MAN and PVK equations are provided on table 1.

Table 1 - Hydraulic Variables Necessary for Estimating Discharge

Both of these equations require an estimate of roughness and an estimate of the height of the channel bottom in the reach from which stage dynamics can be referenced. These equations are provided below in the form used in the algorithm. Note that the flow width (W), the stage or water surface height (H), and the water surface slope (S) are determined from satellite-derived information. There are unknown coefficients in each equation, the roughness, given by the MAN  $n$  and the PVK roughness height ( $y_0$ ); the height of the bottom or height of zero flow (B); and a channel shape coefficient (b) that reflects the relation between change in height and average change in depth (Dingman, 2007). If the value of b is 2, the uniform geometric shape of the channel cross-section would be a parabola, and higher values represent a higher order paraboloid (Dingman, 2007) with a flatter bottom and steeper banks.

$$\text{MAN: } Q = \frac{\left[ W \left( h - B \right) \left( 1 - \left( \frac{1}{1+b} \right) \right)^{1.67} S^{0.5} \right]}{n} \quad (1)$$

where: Q = the river discharge, ( $\text{m}^3/\text{s}$ )

W = the width of flow, (m)

h = the water surface stage (height) above a common datum, (m)

S = the water surface slope between observations of stage

n = the Manning roughness (resistance) coefficient

B = the stage of zero flow, (m)

b = the assumed channel shape coefficient.

$$\text{PVK: } Q = 2.5WY(gYS)^{0.5}(\ln\left(\frac{Y}{y_0}\right) - 1) \quad (2)$$

$$Y = \text{average depth} = (h - B)\left(1 - \left(\frac{1}{1+b}\right)\right), \text{ (m)}$$

$$y_0 = \text{roughness height, (m)}$$

$$g = \text{gravitational constant, } 9.81 \text{ m/s}^2$$

To evaluate the value of the shape coefficient,  $b$  (from eqs. 1 and 2) we accessed a large data set of measured maximum and mean flow depths made by the USGS in river cross-sections across the United States as part of flow measurements made with ADCPs (Canova et al., 2016). The data used included only complete records for each gage with positional information (latitude, longitude, and elevation), drainage area, discharge, width of flow, maximum and mean velocity, maximum and mean depth, and cross-sectional area of flow. The data were quality controlled so that the reported discharge agreed within 5% of the discharge calculated by multiplying the width times the mean depth times the mean velocity. Negative discharges (in tidal reaches) and multiple channel discharge measurements were also excluded from the data used for this analysis. The data were used to examine the “typical” channel cross-section shape as it is reflected by the relation between maximum and mean depth in the cross-section. For example, a value of the ratio max/mean of 1.5 is the value associated with a parabola (2<sup>nd</sup> order parabolic shape), a value of 1.33 is that associated with a 3<sup>rd</sup> order parabolic shape, 1.25 is that associated with a 4<sup>th</sup> order parabolic shape, etc. Fig. 1 shows the maximum depth plotted as a function of the mean depth for over 25,000 river cross-sections obtained from the ADCP data base. The data include a wide range of flow levels in thousands of rivers that ranged in width from less than 30 meters wide up to more than 1,000 meters wide. The relation between the maximum and mean depth is remarkably consistent across all flow levels and rivers, with a Pearson  $r^2$  of 0.97. The slope of the best fit line shown on fig. 1 is 1.48, indicating that the shape of the cross-section is best represented by a parabola.

Figure 1 – Plot of the maximum depth of flow in a cross-section versus the mean depth of flow for 26,228 measured river channel cross-sections in the United States, showing a trend line with a slope of nearly 1.5, which would be the value if the general cross-section shape reflects the characteristics of a parabola. The dotted line represents the best fit line given by the equation shown on the chart with the associated coefficient of determination ( $r^2$ ).

The value of the shape factor,  $b$ , is used to estimate the bottom depth ( $B$ ) of the cross-section from the width and stage observations. Given the assumed parabolic shape of the cross-section ( $b = 2$ ; note also that from geometric considerations, the ratio of maximum to average depth for a parabolic cross-section shape is 1.5), the relation between the width and depth is expressed by the following (Dingman, 2007):

$$Y = aW^2 \quad (3)$$

Where  $W$  is the width and  $Y$  the depth (either mean or maximum) and  $a$  is the coefficient of the parabola (which is defined by the ratio of the maximum depth divided by the maximum width squared

$$(Y_{\max}/W_{\max}^2)$$

Recognizing that  $Y$  can also be expressed as a function of stage, as  $Y = (H-B)$ , the following relation between stage and width is derived

$$H - B = aW^2 \quad (4)$$

Rearranging this equation defines a linear relation where the coefficient  $a$  and  $B$  can be defined by determining the linear trend through regression analysis, with width as the independent variable and depth the dependent variable such that

$$H = aW^2 + B \quad (5)$$

Conversely, given time series of stage and width, a linear relation between stage and width squared can be derived by fitting a straight line regression that allows for the width to be estimated from more frequent observations of stage, such that

$$W^2 = zH + c \quad (6)$$

where the slope of the line,  $z$ , is  $(1/a)$  and the intercept,  $c$ , is  $-(1/a)B$ . In this study, we have developed an observational record of stage for the period 2008 to 2014 from Jason-2 altimeter satellite, and a limited observational record of mean flow width for the reach between Jason-2 satellite tracks based on Landsat imagery. With the limited Landsat imagery we related the stage and width to derive both the value of  $B$  (which represents the bottom, or lowest height, of the assumed parabolic section) with equation 5 and with equation 6 we estimate width from stage for every stage observation.

A relation developed by Bjerklie (2007) was used to derive the roughness coefficients (MAN  $n$ , and PVK roughness height,  $y_0$ ). It estimates bankfull river velocity from the along channel-meander length ( $\lambda_c$ ) and the water surface slope. The estimate of velocity is then used to back calculate roughness values with a statistically derived estimate of the Froude number ( $F_b$ ) for bankfull rivers. The Froude number is the ratio of inertial force (velocity) to the gravitational force (depth) in the flow, and is an index of the relation of kinetic to potential energy. The ratio, in large part, is a function of the resistance or slowing of the flow,

The Bjerklie (2007) relation is:

$$V_b = \sqrt{\frac{2g \lambda_c S}{m}} \quad (7)$$

where  $V_b$  = bankfull velocity

$m$  = fraction of the meander length ( $\lambda_c$ ) that contributes to energy dissipation.

The length  $\lambda_c/m$  is referred to here as the resistance length,  $L_r$  and can be calculated according to Bjerklie (2007) by:

$$m = 9.67(\lambda_c S)^{0.36} \quad (8)$$

The Froude number relation is developed from a set of bankfull river data (Bjerklie, 2007;  $N = 521$ , assembled from Barnes, 1967; Church and Rood, 1983; Dingman and Palaia, 1999; Osterkamp and Hedman, 1982, and Schumm, 1960, that includes rivers in the United States, Canada, and the United Kingdom) using log-linear regression of  $F_b$  versus water surface slope, provided below:

$$F_b = 2.85(S)^{0.31} \quad (9)$$

The Bjerklie (2007) analysis of Eq. (9) resulted in an  $r^2 = 0.42$ . The data are plotted in fig. 2. The Froude numbers predicted by Eq. (9) are similar in magnitude as those predicted by equations proposed by Grant (1997) for channel slopes less than 0.01 that were derived for gravel and sand bed rivers. The P-value ( $<0.00001$ ) for the relation indicates that the value of the coefficient and exponent in the relation given by Eq. (9) are significant at the 95% confidence level.

Figure 2 - Relation between  $F_b$  and slope (data from Bjerklie, 2007;  $N = 521$ , assembled from Barnes, 1967; Church and Rood, 1983; Dingman and Palaia, 1999; Osterkamp and Hedman, 1982 and Schumm, 1960, that includes rivers in the United States, Canada, and the United Kingdom). The line is the best fit given by equation (9), with a coefficient of determination ( $r^2$ ) of 0.42 .

According to Bjerklie (2007), the value of the bankfull Manning  $n$  ( $n_b$ ) is computed by calculating the bankfull velocity ( $V_b$ ) by the following, which is derived by combining eqs. (7) and (8):

$$V_b = 1.37(\lambda_c S)^{0.32} \quad (10)$$

An initial bankfull depth ( $Y_b$ ) is then computed according to Eq. (9) given that the bankfull Froude number is equal to  $\frac{V_b}{\sqrt{gY_b}}$ . The equation for the bankfull roughness coefficient is expressed by rearranging the classical Manning velocity expression:

$$n_b = \frac{Y_b^{0.67} * S^{0.5}}{V_b} \quad (11)$$

As presented in Chow (1959) for a given constant state of flow, the Manning  $n$  is related to the roughness height in the PVK equation and can be estimated from the following relation, which indicates that the Manning  $n$  (flow resistance) is a function of flow depth:

$$n_b = \frac{Y_b^{0.17}}{22 * \log\left(\frac{Y_b}{y_0}\right) - 8.6} \quad (12)$$

The estimate of the roughness height used in the PVK equation is a constant for all flow levels. However the scalar effect on discharge is determined by the ratio of depth to roughness height, i.e. the relative

roughness. The roughness coefficient used in the MAN equation ( $n$ ) does not explicitly account for the concept of relative roughness. As a result most studies of the variation of Manning  $n$  show that its value varies with depth and flow (e.g. Hicks and Mason, 1991; Coon, 1998). To account for variation in the Manning  $n$  with depth, we adopt a logarithmic scalar that relates the bankfull Manning roughness coefficient ( $n_b$ ) to the ratio of maximum stage height difference ( $H - B$ ) to observed stage height difference ( $h - B$ ) (Limerinos, 1970; Jarrett, 1984) where  $H$  is the stage height estimated for the bankfull flow state,  $h$  is the stage height at the time of the observation, and  $B$  is the stage height at zero flow (the bottom). The scaled value for Manning  $n$  is given by:

$$n = n_b \left(1 + \log \left(\frac{H-B}{h-B}\right)\right) \quad (13)$$

### 2.3 Selection of Reach based on Meander Length

An important consideration with this method is the reach length over which the slope, average width, and meander length is estimated. If the reach is too long, it may include significant changes in morphology and discharge. If the reach is too short, measured variables are not representative of the energy balance in the reach as a whole. This latter issue could introduce greater local variation than is representative of the energy and backwater regime in the channel, i.e. the hydraulic control. Bjerklie (2007) showed that the reach length over which the energy dissipation maintains a stable flow state is reflected by the meander length and the channel slope.

An interesting parallel to this concept was presented by Moody and Troutman (2002) who proposed a concept they called the integral length ( $L_i$ ). The integral length is defined here as the downstream length over which a hydraulic variable in the reach for a given discharge can be suitably averaged and represented as a constant. It is similar to the idea of a statistically stationary dynamical river meandering



process on the reach scale that depends on upstream and downstream conditions in the channel (Camporeale et al., 2005). Values for  $L_i$  (m) are typically 1 to 2 channel widths in length and can be calculated by the following relation with the mean discharge ( $Q_a$ ,  $m^3/s$ ) as proposed by Moody and Troutman (2002):

$$L_i = 14Q_a^{0.54} \quad (14)$$

$L_i$  is strongly correlated with the resistance length ( $L_r$ ), as shown on fig. 3 for a set of 48 rivers with sufficient data to estimate both length scales (data from Bjerklie, 2007). Considering the error in estimating the mean and bankfull discharge values for the sample data set, the correlation between  $L_i$  and  $L_r$  is considered to be highly significant. This suggests that  $L_i$  and  $L_r$  are both independent measures of the same phenomenon, namely the length over which the reach attains its most probable state, which is reflective of the energy dissipation processes that form the channel reach regime.

*Figure 3 – Plot showing the comparison between the resistance length,  $L_r$  (Bjerklie, 2007) and the integral length,  $L_i$  (Moody and Troutman, 2002). The dotted line represents the best fit line given by the equation shown on the chart with the associated coefficient of determination ( $r^2$ ).*

As a result of these considerations, we calculated the necessary minimum reach length ( $L_i$  and  $L_r$ ) to be (approximately) 1 and 2 km, respectively, at the two locations. These include the approximate range of twice the bankfull channel width of the Yukon River at both stations. However, due to constraints of the satellite ground track locations (see section 2.4), the maximum length over which we could average hydraulic variables and derive discharge is dictated by the upstream and downstream satellite overpasses. The reach lengths prescribed by the ground track locations are much longer than the minimum required based on the above considerations. This is not considered to be an issue provided there are no significant tributary inputs or hydraulic controls within the length of river reach used for determining the slope.

Based on the imagery, no other significant tributaries or hydraulic controls exist with the reaches observed in this study.

#### 2.4 Water Surface Stage and Slope from Satellite RADAR Altimetry

Full details of the principles of satellite radar altimetry can be found elsewhere (Fu and Cazenave, 2001) and specifically to its application to inland water in a number of early texts (e.g., Birkett, 1995; Birkett, 1998). In brief, the technique relies on the emission and reception of a microwave pulse that is transmitted to the surface. Timing the echo allows the distance to the surface (or “Range”) to be estimated.

Combining the Range distance with knowledge of the satellite’s altitude, and applying a number of instrument-related and geophysical corrections, leads to the derivation of the surface height with respect to a reference datum. Historic and current radar altimeter missions revisit the same point on the earth’s surface every 10 to 35 days, depending on the mission. The advantages of satellite radar altimetry include day/night and all-weather capability with little hindrance due to canopy or vegetation cover. Limitations include the ability to only record height measurements at nadir (directly below the satellite), failure to acquire the surface in complex or rugged terrains, restrictions on “target” size due to a variety of factors, and potentially erroneous height data due to penetration effects into snow and ice. During ice-free periods, inland water surface height accuracies have been found to vary from centimeters to several decimeters.

The NASA/CNES Jason-2 Ocean Surface Topography Mission (Jason-2/OSTM) has an on-board radar altimeter (Poseidon-3) that operates at 13.575-GHz (Ku-band), and covers the globe within  $\pm 66^\circ$  latitude. In the initial phase of the satellite mission, each repeat-pass had an associated ground track where the same location on the surface was revisited to  $\pm 1$  km (a mission requirement, in practice this was a more confined  $\pm 250$  m). Like its predecessors TOPEX/Poseidon and Jason-1, Jason-2

revisited the same point on earth every 10 days. The duration of the Jason-2/OSTM mission enabled 303 ten-day repeat cycles spanning the July 2008 to October 2016 period.

To assist with coastal and inland water programs, new tracking modes were implemented into the Poseidon-3 operating strategy to help acquire and re-acquire the surfaces quickly in complex terrains and especially at land/water boundaries. In addition, enhanced post-processing of the radar altimeter echoes provided several Range estimate options to improve accuracy for a variety of surface types. Inland water studies (e.g., Birkett and Beckley, 2010) showed that the DIODE acquisition/Median Tracking mode and the DIODE/DEM mode were reliable over river and lake surfaces, and that the Range option based on output from the ice echo-retracker algorithm also served river/lake surfaces well.

The Jason-2/OSTM Geophysical Data Record (GDR) data set

( <ftp://ftp.nodc.noaa.gov/pub/data.nodc/jason2/> ) provided satellite altitude, altimetric Range measurements, and computed latitude/longitude at a rate of 20-Hz, i.e., every 290 m along the ground track, with geophysical range and height corrections at the lower 1-Hz rate. For the reconstruction of surface water level heights over rivers the processing selects the Range parameter deduced from the ice-retracking algorithm, and the model-based atmospheric Range correction parameters which account for microwave propagation delays due to water vapor and ions. Reconstructed water level heights at this point in the processing are geodetic i.e., based on a reference ellipsoid datum, in this case one created for the earlier TOPEX/Poseidon mission.

The Google Earth application (use of trade, firm, or product names is for descriptive purposes only and does not imply endorsement by the U.S. Government) and access to the Jason-2/OSTM reference ground track dataset (AVISO 2016) allows for detailed viewing of the satellite overpass locations with respect to the river reach crossings. For the Yukon, river reaches were selected based on the Jason-2/OSTM

overpasses in proximity to the USGS streamgage locations at Eagle and Stevens Village. In each case, a pair of satellite crossings were sought, one upstream and the other downstream of the USGS gage. The resulting crossing pairs were identified as pass251/pass204 for Eagle and pass227 for Stevens Village. The Stevens site requires only one Jason-2 satellite overpass because of the orientation of the river in relation to the orbital path (fig. 4) and thus the upstream and downstream crossings are performed on the same day in each repeat cycle. For the Eagle site there is a 2-day offset between the upstream and downstream crossings. Fig. 5 shows the Jason-2 satellite ground tracks relative to the Yukon River reaches at Eagle, Alaska. Figs. 4 and 5 also show the passes for the ICESat satellite described in the subsequent section.

*Figure 4 – Jason-2 (white pushpins) and ICESat (yellow pushpins) satellite crossing locations on the Yukon River reach near Stevens Village, Alaska. Jason-2 pass227 crosses both upstream (j.pass.227.1) and downstream (j.pass.227.2) of the USGS streamgage site near Stevens Village (latitude 65.87 deg. W, longitude 149.72 deg. N marked by red circle.) ICESat pass 0342 (upstream), and passes 0223 and 0334 (downstream), are utilized in the study.*

*Figure 5 - Jason-2 (white pushpins) and ICESat (yellow pushpins) satellite crossing locations on the Yukon River reach at Eagle, Alaska. Jason-2 pass 251 and ICESat passes 0297 and 1279 are upstream of the USGS gage site at Eagle (latitude 64.79 deg. W, longitude 141.2 deg. N marked by red circle). Jason-2 pass204 and ICESat passes 0044 and 0178 are downstream crossings. Due to overpass orientations and river meandering, ICESat pass 0289 strikes the river at five different locations but valid heights were only found on the upstream reach.*

Noting the location of the river-bank crossings on each satellite pass, the altimetric heights were first checked for quantity and quality before being used to determine a first approximation of the reach height, and its variability with respect to the satellite-based datum. With 303 cycles of data (July 2008 to October

2016), a form of repeat-track methodology (Birkett, 1998) was then applied to construct a time series of water level variations at each reach crossing. For each overpass location, this methodology relies on the selection of one overpass (i.e. one cycle with a given date/time) as a reference pass and compares all others to it. The result is a time series of water level variations based on an arbitrary datum.

The Jason-2 time series of relative water level variations was filtered to remove any variation with an error bar greater than or equal to 0.5m. Manual inspection of the bank-to-bank height profiles across each reach allowed further rejection of data points where the automatic data filtering failed. At 10-day resolution, the final time series (figs. 6 and 7) reveal seasonal and inter-annual variations across the ~8-yr satellite period, but not the higher frequency fluctuations. The relative stage variations were then converted back to the original reference ellipsoid datum and a geoid correction applied (based on the EGM2008 gravity model employing 30arc second or 1km resolution) to bring the stage values into an orthometric frame. For each satellite repeat cycle, the resulting heights were then differenced between the upstream and downstream locations, and the result divided by the reach thalweg, to form a slope for that section. Representative results are shown on table 2. The listed preliminary thalweg distances, i.e. following the river center between overpass pair locations, were formed from an average of three measurements utilizing Google Earth imagery. These thalwegs automatically carry an associated  $\pm 500\text{m}$  error due to variations in the ground track location caused by satellite orbit drift. The first-order slopes were derived via non-interpolation of the Eagle reach satellite heights to account for the 2-day difference in overpass date. The resulting reach slope at Eagle (mean=0.000312) and Stevens Village (mean=0.000091) show little variability across the 8 years of Jason-2 observations (figs. 6 and 7, see following sections), with good stability between March and November (for Eagle), and between May and October (for Stevens Village) even though during some of these periods the river may still be frozen.

Table 2 – Jason-2 and ICESat comparative observations

*Figure 6 – Seasonal Jason-2 water surface slopes Yukon River near Stevens Village, Alaska, for the reach between the upstream and downstream river crossings for pass227 over the eight year observation period – each color symbol represents a different year. Winter (November to April) slope estimates (small triangles) with greater scatter due to snow/ice penetration effects, are distinguished from those derived during the late spring through fall period (squares). The limited multi-year ICESat winter water surface slopes (green asterisks) which should not suffer from ice/snow penetration effects, are biased ~14% higher than the mean summer slope observed by Jason-2.*

*Figure 7 – Seasonal Jason-2 water surface slopes Yukon River at Eagle, Alaska, for the reach between the upstream and downstream river crossings (Pass 251 and Pass 204) over the eight year observation period – each color symbol represents a different year. Because of potential ice/snow penetration, slope estimates during a slightly shorter (December through April) winter season (small triangles) are rejected when estimating a mean reach slope value. Biased ~7% lower than this mean is the average of the multi-year multi-season ICESat water surface slopes (green asterisks) which should not be affected by snow/ice penetration.*

## 2.5 Stage, Thalweg Height and Slope from Satellite Laser Altimetry

Laser altimetry (lidar) is a mature technique employed for surface mapping, trading poor temporal repeatability for high spatial resolution. The majority of vehicles for operation are airborne, though lidars have been deployed on two low-Earth orbit NASA Shuttle missions (SLA01, SLA02), and one space-based NASA (ICESat) mission. Examples of satellite lidar application to inland water bodies can be found in a number of texts (e.g., Harding and Jasinski, 2004; Calmant et al., 2004; Birkett et al., 2005; Carabajal et al., 2006; Birkett et al., 2010; Zhang et al., 2011; Boy and Carabajal, 2013; Srivastava et al., 2013; Wang et al., 2013). The technique relies on the emission and reception of an optical wavelength laser-derived pulse and the measurement of the Range distance as derived from the timing of the returned

energy distribution (the laser waveform) of the surface scattering elements (Harding and Carabajal, 2005). The first satellite lidar mission, ICESat, has utilized lidar, operating a primarily nadir-viewing instrument, and providing height information along a reference ground track. The ICESat mission advantages included day/night operation with a much smaller footprint than the satellite radar altimeters. In addition, operating at infrared wavelengths there was no penetration into the surface of snow or ice, and so winter water elevations were unbiased. Limitations of the ICESat data include a (mainly) nadir-viewing operation, failure to acquire the surface under certain optically thick cloud cover conditions, and laser waveform saturation effects. Cloud cover can lead to forward scattering effects that translate into delays on the Range measurement. Such conditions can often be identified and corrected for via the use of cloud flags and corrections derived from cloud products (Spinhirne et al., 2005). Saturation effects occur when the peak power of the returned signal from snow and ice surfaces is found to span a wider dynamic range than planned, often exceeding the linear dynamic range of the 1064nm detector assembly (Sun et al., 2017; Abshire et al., 2005). During ice-free periods, inland water surface height accuracies have been found to be in the centimeter to several decimeters range.

The ICESat mission operated between 2003 and 2009 with a primary objective of mapping ice sheets and sea ice (Zwally et al., 2002). The Geoscience Laser Altimeter System (GLAS) consisted of 3 lasers which could operate at infrared (1064nm) and visible (532nm) wavelengths. With an effective footprint size of ~70m ICESat was placed in a 91-day repeat mapping orbit (with a 33-day sub-cycle) with global coverage extending to  $\pm 86^\circ$  latitude. Most of the operating periods were split between the February-March, and September-December periods, although three campaigns were undertaken during May-June. While this limits its utility for observation of river stage and surface slope, the variability allows some measure of surface slope cross-validation with the radar altimeter derived slope estimates.

The ICESat data was processed into a number of different Level 1 and 2 data sets depending on the end user requirement. For this study, version 34, GLA14 (Level 2) altimetric parameters based on 1-Hz and

40-Hz along-track resolution were used. The GLA14 altimetric Range parameter is corrected for atmospheric effects. The reconstructed surface height values are corrected for tidal effects resulting in one value every 175 m along the ground track that were further corrected for saturation effects. Similar to the radar missions, reconstructed water level heights are geodetic and based on the TOPEX/Poseidon reference ellipsoid datum.

In addition, cloud detection is applied using a combination of pulse width, amplitude, and waveform peak magnitude checks, as well as examining deviations from the expected elevation based on the SRTM or GTOPO30/GMTED elevation models. The isolation of the river reaches from the surrounding land was initially tested using a number of water masks but ultimately relied on Google Earth imagery. The initial ICESat data processing focused on a large set of available satellite overpasses though after data quality/quantity assessments the final satellite pass pairs selected were based on upstream (0297, 0289, 1279) and downstream (0044, 0178) ICESat passes for the Eagle reach, and upstream (0342) and downstream (0223, 0334) passes for the Stevens reach. ICESat passes 0289 and 0342 crossed the Yukon River at multiple locations due to meandering, but only a few locations had success in stage retrieval (figs. 4 and 5).

Overpass locations, thalwegs, and derived reach slopes (again based on the EGM2008 geoid model) are presented in table 2 and on figs 4, 5, 6, and 7 along with comparative Jason-2 observations. Note that the ICESat measurements were primarily March/April and October/November observations, and compared to Jason-2, the ICESat thalweg distances and the temporal difference between the overpass pairs (7-41 days) were larger. Despite these differences ICESat slopes are comparable to those observed by Jason-2 and thus provide some form of validation of the radar measurements. However, ICESat slopes are biased ~7% lower at Eagle, and ~14% higher at Stevens Village. The fact that there is not a constant (inter-mission) slope bias between the radar and lidar results (ICESat slopes are biased ~7% lower at Eagle and ~14% higher at Stevens Village), suggests physical (site locations and thalwegs) influences could be playing a



role, though differences in applied altimetric corrections could also be contributing. These will be explored in greater detail in a later study.

## 2.6 Water Surface Width, Stage-Width Relationships, and Meander Length from Optical Satellite

### Data

Surface water width and meander length were derived using satellite optical data collected by Landsat. A provisional USGS product ([https://remotesensing.usgs.gov/ecv/SWE\\_overview.php](https://remotesensing.usgs.gov/ecv/SWE_overview.php); Jones, 2015 Jones, 2017) named Dynamic Surface Water Extent (DSWE) is designed to detect land surface inundation in Landsat data pixels that are unobscured by clouds, cloud shadows, or snow (note: The DSWE software is provisional and is subject to revision. It is being provided to meet the need for timely best science. The software has not received final approval by the U.S. Geological Survey (USGS). No warranty, expressed or implied, is made by the USGS or the U.S. Government as to the functionality of the software and related material nor shall the fact of release constitute any such warranty. The software is provided on the condition that neither the USGS nor the U.S. Government shall be held liable for any damages resulting from the authorized or unauthorized use of the software.). Although the DWSE product is provisional and its preliminary results can be used to highlight the total water extent along a river reach. We used the provisional DSWE product to determine cross-sectional distances to formulate an average reach width. For this pilot study, 8 Landsat 5 images (table 3, table 4) were processed to determine total open water extent for reaches of river at the USGS Stevens Village streamgage (fig. 8) and the Eagle streamgage (fig. 9) during the Jason-2 operating period (2008 – 2016). These particular Landsat scenes were selected to minimize the amount of cloud and snow cover and span dates of radar altimetry, although the dates of the images were not necessarily coincident with radar altimetry data collection. Although DSWE can be generated for any scene in the Landsat Archive, the number of scenes chosen for this pilot were sufficient to develop an initial correlation between stage and width to demonstrate an initial rating for the river channel.

*Figure 8 – Landsat image of the Yukon River near Stevens Village, Alaska, showing the Stevens Village streamgauge (red circle, latitude 65.87 deg. W, longitude 149.72 deg.) and the water surface extent in the river channel determined from DSWE in blue-green. The flow direction is to the left.*

*Figure 9 – Landsat image of the Yukon River at Eagle, Alaska, showing the Eagle streamgauge (red circle, latitude 64.79 deg. W, longitude 141.2 deg.) and the water surface extent in the river channel determined from DSWE in pink. The flow direction is towards the top of the image.*

The Landsat pixel resolution is 30 m. The DSWE model uses digital elevation data and a cloud mask to avoid misclassified pixels in terrain and cloud shadows. Cloud and cloud shadow masking was performed using the technique developed by Zhu and Woodcock (2012). The data were delivered in Universal Transverse Mercator projection, in a Hierarchical Data Format Version 4 (HDF4), and included 11 bands of information. Of the 11 bands, six bands were surface reflectance data now distributed by the USGS as a Higher Level product ([https://landsat.usgs.gov/sites/default/files/documents/lasrc\\_product\\_guide\\_ee.pdf](https://landsat.usgs.gov/sites/default/files/documents/lasrc_product_guide_ee.pdf)). Another band was a cloud, cloud shadow, and snow mask. The final four bands contained: DSWE layer without any masking performed; one with cloud, cloud shadows, and snow removed using the cloud mask; a third in which terrain data were used to eliminate areas shaded by topography; and finally the terrain data used for the topographic shadow correction.

For this study we chose the classes provided in the cloud, cloud shadow, snow, and terrain corrected DSWE data that were representative of water. For ease of calculating cross-section distances along the Yukon River, the water pixels were converted to vector polygons. The polygon data allows us to isolate the river channel from lakes, wetlands, and smaller watercourses in the Landsat data. Tables 3 and 4 show estimated river width (area divided by reach length) for Stevens Village and Eagle reaches, respectively.

They also show the mean of observed and interpolated (average of upstream and downstream) Jason-2 and USGS gage heights for each reach on the days of each image. At the Eagle station, to obtain concurrent observations at the upstream and downstream locations, the gage heights were linearly interpolated between observations so that the upstream and downstream observation each had a concurrent interpolated height coinciding with the date of each observation.

Table 3 – Landsat Image Analysis Data for the Yukon River Stevens Village Reach

Table 4 – Landsat Image Analysis Data for the Yukon River Eagle Reach

The data in tables 3 and 4 were used to construct a unique stage-width relation for each reach, and this relation was used to estimate an effective river width for the channel associated with each water surface height observed by Jason-2. The stage-width relations are shown on figs. 10 and 11. These relations are considered to be approximate due to the small data set used. However, they provide an illustration of the method, and given the large number of scenes in the Landsat Archive, would be expanded to include many more data points in future applications. Additionally, these limited data illustrate that channel relations between stage and width can be developed and applied even where usable Landsat images may be few in number due to pervasive cloud cover (for example).

*Figure 10 – Relation between Jason-2 average of the upstream and downstream observed stage and squared value of the average reach width for the Yukon River near Stevens Village, Alaska. The dotted line represents the best fit line given by the equation shown on the chart with the associated coefficient of determination ( $r^2$ ).*

*Figure 11 – Relation between Jason-2 average of the upstream and downstream observed and interpolated stage and the squared value of the average reach width for the Yukon River at Eagle, Alaska. The dotted line represents the best fit line given by the equation shown on the chart with the associated coefficient of determination ( $r^2$ ).*

The reach water surface area was also used to estimate the meander length of the river near the gages. The meander length was defined according to methods outlined in Bjerklie (2007), by subdividing the reach into 2 km sections, plotting the center points of these sections, and determining points of inflection. The derived meander lengths (38.3 km for the Stevens Village site, and 34.7 km for the Eagle site) are validated by the preliminary values (36.8 km and 34.5 km respectively) reported in table 2, and so are utilized here, and are considered a constant across the 2008-2016 study period.

## 2.7 Calibration of Discharge

A calibration approach that adjusts high and low bias as well as reduce the mean bias was used in order to compare with the uncalibrated estimate as well as demonstrate a practical calibration method. The method is considered to be practical by minimizing the need for establishment of a ground-based gaging station, but still requiring minimal ground data collection consisting of at least three independent ground measurements of discharge. The calibration adjusted the flow resistance to match three discharge measurements at each site that represented the low, mid, and high end of the range of discharge. The calibration was only performed for the MAN because the variation in flow resistance with depth (and discharge) could easily be characterized by a variable power function, as demonstrated by Ferguson (2007). Theoretically, the PVK equation assumes that the roughness height (which controls the flow resistance) is a constant under all flow conditions and varies as a logarithmic function of relative depth, and therefore inclusion of a secondary relation to account for an alternative variation in flow resistance

would be more problematic. No such theoretical limitation exists for the MAN equation. For this reason, the PVK equation was not calibrated.

The three independent discharge measurements used for calibration, as previously mentioned, included a high, mid, and low discharge range (arbitrarily selected from USGS discharge at each gage) and these were compared against the discharge estimates made using the MAN equation for the same dates. The calibration proceeded by fitting a power function to adjust a base value for the Manning  $n$  ( $n_b$ ) which is then used to calculate the dynamic value of Manning  $n$  according to the following:

$$n = n_b \left( \frac{H-B}{h-B} \right)^x \quad (15)$$

The value of  $n_b$  is adjusted to fit the mean of the three USGS discharge estimates with the mean of the three comparable MAN estimates, addressing the bias on the mean. Then, the exponent  $x$  in equation (9) is adjusted to match the coefficient of variation of the three USGS ground measurements with the three MAN estimates, addressing the high and low bias.

### 3.0 Results

Time series of discharge were estimated from the remotely sensed widths, stages, and slopes using the MAN and PVK equations. Note that the estimate of discharge also results in estimates of mean depth and mean velocity of flow. The estimate of depth follows directly from the channel cross-section geometry that is determined from the remote observations of width and stage (with the maximum observed stage considered to represent the bankfull stage), coupled with the assumption of a parabolic cross-sectional shape. Fig. 12 A and B show the assumed cross-section compared to a USGS cross-section for the Stevens Village and Eagle streamgages, respectively, measured during a similar magnitude of discharge.

The cross-section shape at Stevens Village is markedly different than the assumed parabolic section that conveys the same discharge, indicating that the estimate of mean depth associated with a given observed width and stage may vary considerably from the reality, and as a consequence also the mean velocity. The cross-section comparison at Eagle is less markedly different. The assumption of the parabolic cross-section shape is meant to represent the channel reach, and may show more or less comparability to the reality for any given cross-section in the reach. Irrespective of the reach versus cross-section variability, the parabolic assumption is recognized to be a convenient representation of the actual channel cross-section, and may be improved over time as more field data are gathered.

*Figure 12 – Comparison between the cross-section shape measured by the USGS at the Stevens Village (A) and Eagle (B) streamgages and the mean channel cross-section that is derived from the assumed parabolic cross-section shape for a similar discharge.*

Two discharge estimates were derived, one uncalibrated that uses all of the measured and derived information shown on table 1, and as such is completely estimated from remotely measured variables, using equations 5, 6, 7, 8, and 9; and a second estimate that calibrated the Manning roughness coefficient. The other estimate was calibrated to three USGS measured discharges as described in section 2.7. Using the calibration procedure, the Manning  $n$  values for the Stevens Village reach ranged from 0.025 (the bankfull value) and 0.053 with a mean of 0.040, and for the Eagle reach ranging from 0.024 to 0.062 with a mean of 0.037.

The accuracy of the reach-averaged river widths derived from Landsat could not be evaluated independently because there was no comparable reach averaged width measured in the field and the development of independent accuracy assessment data was beyond the scope of this pilot project. The accuracy of the satellite stage measurements also is not direct, but were compared directly with stage measured at the USGS streamgages, by averaging the satellite observations of the river water surface

upstream and downstream of the streamgage. Water surface slopes are not measured at the USGS gages, and therefore there is no direct comparison for the altimeter derived slope values.

### 3.1 Results for the reach near USGS Gage near Stevens Village

Water surface height observations made by the Jason-2 satellite altimeter, collected for the period August 9, /2008 to October 1, 2016, are compared against water surface stage measurements collected by the USGS at the Yukon River near Stevens Village gaging station. The USGS stage readings are published as a height above an elevation datum referenced to NAVD88. The Yukon River reach near Stevens Village, Alaska is shown on figs. 4 and 8. Observations for the winter (November 1 to April 30) were not included in the data (to avoid the possibility of ice on the surface water) and also were not included for periods when USGS data were not available, resulting in 90 observations over the 8 year period.

The water surface height observations made by Jason-2 upstream and downstream of the USGS Stevens Village gage were averaged to compare against the USGS stage height at the gage. Fig. 13 shows that the comparative dynamic change in height are very similar and that the two observations are in good agreement. Table 5 shows the comparative statistics between the USGS stage and the Jason-2 stage.

Table 5 - Stage Statistics for Yukon River near Stevens Village, Alaska

*Figure 13 – Average Jason-2 (average of upstream and downstream) and USGS river heights for the Yukon River reach near Stevens Village, Alaska, (A) over the 8 year period and (B) showing the linear one-to-one line.*

Fig. 14 shows the Jason-2 pass227 (refined thalweg=38.3km) water surface slope variation over time for the Stevens Village reach. Slope estimates made in the field by Clement (1999) indicate that the river

reach downstream of the Yukon Flats and upstream of Stevens Village averages about 14 cm/km (0.00014), with a range of 1 to 32 cm/km (0.00001 to 0.00032). The Jason-2 slope measurements average 9.1 cm/km with a standard deviation of 1.4 cm/km and a range of 3 to 14 cm/km. The Jason-2 slope measurements are well within the range observed by Clement (1999). The multi-year Jason-2 observations enables an assessment of slope change over time and its relation to other observed hydraulic variables.

*Figure 14 – Jason-2 observed water surface slope variation over time for the Yukon River reach near Stevens Village, Alaska.*

The estimated discharge for the river reach using the MAN and PVK equations and the measured USGS discharge at the gage are shown in fig. 15 A and B. Fig. 15 C shows the calibrated estimates plotted against the USGS values, and fig. 15 D shows the stage-discharge relation between the Jason-2 water heights (adjusted to the USGS datum) and the calibrated estimated discharge compared to the stage-discharge relation derived from USGS measured stage and discharge.

*Figure 15 – Estimated uncalibrated river discharge using the (A) MAN and the (B) PVK equations compared to the USGS measured discharge for the Yukon River reach near Stevens Village, Alaska; the calibrated estimated discharge versus USGS discharge for the MAN equation (C) and the calibrated stage-discharge relation for the estimated discharge compared to the USGS measured stage-discharge relation (D).*

Table 6 provides the statistical comparison between the USGS measured discharge and the discharge estimated from the MAN and PVK equations. The absolute value of one minus the antilog of the log error is approximately the percent error of the log residuals. The table shows both the uncalibrated statistics, where the roughness coefficients were determined from the various hydraulic relations, and the calibrated



statistics, where the roughness coefficients are adjusted so that the mean of the estimates matches the mean of the comparable USGS measured discharge. For the uncalibrated estimates, the mean error ranges from 5 to 13% (depending on log or absolute) for the MAN equation and 3 to 8% for PVK. Examining figs. 15A and B shows some bias at the high and low end of the discharge range for the uncalibrated estimates. The calibrated estimates (fig. 15 C) show that the mean bias and the bias at the high and low end are nearly eliminated. The Nash-Sutcliffe statistic and the normalized root mean square error (measures of goodness of fit over the entire time series) show good results for both the MAN and PVK, with MAN showing slightly better results. The calibrated estimates for the MAN equation show improvement in all statistical measures, with the mean error of 1%.

Table 6 - Discharge Statistics Yukon River near Stevens Village

The methods used to estimate discharge, because they are based on a physical hydraulic relation, yield estimates of width, depth, and velocity in addition to discharge. After calibration, the estimated mean depth, discharge, and velocity are compared to USGS values for comparable discharge. For the MAN equation at a discharge of  $6,971 \text{ m}^3/\text{s}$ , the estimated mean depth is 8.7 m and mean velocity is 1.2 m/s. This compares with a mean depth for the USGS streamgage of 7.8 m and a mean velocity of 1.4 m/s for a discharge of  $7,172 \text{ m}^3/\text{s}$ . The mean width in the reach derived from Landsat is 644 m whereas the mean width at the gage is 630 m. The differences between the estimated depth and velocity for the channel and the measured depth and velocity at the USGS gage are consistent with the difference in cross-section shape shown on fig. 12.

### 3.2 Results for the reach near USGS Gage at Eagle

Water surface height observations made by the Jason-2 satellite altimeter, collected for the period September 29, 2008 to October 2, 2016, are compared against water surface stage measurements collected

by the USGS at the Yukon River at Eagle gaging station. The USGS stage readings, published in meters (feet) above an elevation datum referenced to NGVD29 located at the gage, are converted to height by adding the stage height to the elevation of the datum. The Yukon River reach at Eagle, Alaska is shown on figs. 5 and 9.

The Jason-2 satellite upstream and downstream crossings of the Yukon River reach at Eagle, Alaska, due to the orientation of the river channel, are not concurrent in time, but ~2 days apart (fig. 5). Under most flow conditions, the stage does not vary widely over a 2-day period, and is assumed to vary uniformly over the period. With a more accurate 34.7 km thalweg, and by interpolating the Jason-2 heights to concurrent dates and restricting the observations further to May 1<sup>st</sup> to October 31<sup>st</sup>, more refined water surface slopes (than section 4.2.1) were estimated. Winter observations were excluded to avoid the possibility of ice on the surface water, and to match periods when USGS data were available. This resulted in 246 final observations over the 8-year period.

The orthometric (section 2.4) water surface height observations and date interpolated heights made by Jason-2 upstream and downstream of the USGS Eagle streamgage were averaged, assuming equidistant upstream and downstream of the gage, to compare against the USGS stage height at the gage. Fig. 16 below shows that the comparative dynamic change in height are very similar and that the two observations are in good agreement. Table 7 shows the comparative statistics between the USGS stage and the Jason-2 stage (average of upstream and downstream heights). However, the magnitude of the differences between the USGS and average Jason-2 heights is greater than observed at Stevens Village, which may be due in large part to the approximate USGS datum referenced to NGVD 1929. The comparison between the USGS and Jason-2 heights also show greater range of difference rather than a consistent bias, which may indicate that there are larger errors in the radar altimeter measurements at this station. Nonetheless, the mean Jason-2 slope is 3.1 cm/km (0.00031) with a range of 2.5 to 3.9 cm/km

(fig. 17). For comparison, Clement (1999) reports the slope at Eagle to be 3cm/km (0.0003) ranging from 0.1 to 5 cm/km indicating that the Jason-2 slope is well within expected values.

Table 7 - Stage statistics for Yukon River at Eagle, Alaska

*Figure 16 – Average Jason-2 (average of upstream and downstream) and USGS river heights for the Yukon River reach at Eagle, Alaska, over the 8 year period (A) and (B) showing the linear one-to-one line.*

*Figure 17 – Jason-2 observed water surface slope variation over time for the Yukon River reach at Eagle, Alaska.*

The estimated discharge for the Yukon River at Eagle using the MAN and PVK equations are compared with the USGS measured discharge are shown on fig. 18 A and B. Fig. 18 C shows the calibrated estimates plotted against the USGS values and fig. 18 D shows the stage-discharge relation between the Jason-2 water heights and the calibrated estimated discharge compared to the stage-discharge relation derived from USGS measured stage (adjusted to the Jason-2 datum) and discharge.

*Figure 18 – Estimated uncalibrated river discharge using the MAN and the PVK equations (A and B) compared to the USGS measured discharge for the Yukon River reach at Eagle, Alaska; the calibrated estimated discharge versus USGS discharge for the MAN equation (C) and the calibrated stage-discharge relation for the estimated discharge compared to the USGS measured stage-discharge relation (D).*

Comparative statistics for the discharge estimates are provided on table 8. The table shows both the uncalibrated statistics, where the roughness coefficients were determined from the various hydraulic relations, and the calibrated statistics where the roughness coefficients are adjusted so that the mean of the

estimates matches the mean of the comparable USGS measured discharge. For the uncalibrated estimates, the mean error ranges from -12 to -21% (depending on log or absolute) for the MAN equation and -6 to -11% for PVK. Figs. 18 A and B show bias at the high and low for the uncalibrated estimates that is more pronounced than was seen at Stevens Village. Similar to Stevens Village, the calibrated estimates show a marked reduction in the bias at the high and low end and in the mean. The Nash-Sutcliffe statistic shows acceptable results for the MAN and poor results for the PVK, and the normalized root mean square error is acceptable for both the MAN and PVK. The calibrated estimates for the MAN equation show marked improvement in all statistical measures with mean error of 2%.

Table 8 - Discharge Statistics Yukon River at Eagle

Similar to Stevens Village, using the three calibration discharges, we directly compare the depth, discharge, and velocity with the comparable USGS values. The mean estimated depth and calibrated discharge and velocity from the MAN equation are 5.4 m, 5,084 m<sup>3</sup>/s and 1.7 m/s respectively. This compares with a mean depth for the USGS streamgage of 5.1 m and a mean calibrated discharge and velocity of 4,487 m<sup>3</sup>/s and 1.8 m/s, respectively. The mean width in the reach derived from Landsat is 532 m whereas the mean width at the gage is 455 m consistent with the difference in mean discharge.

#### 4.0 Discussion

This paper demonstrates the application of remote sensing observations to the estimation of river discharge, but also illustrates the limitations of the approach. Because of the resolution of the Landsat imagery, rivers less than 30 meters in width would not be expected to be discernable. Even if the river could be distinguished from the surrounding landscape, narrower channels would have greater uncertainty in estimates of width due to the relative width to resolution ratio (Bjerklie et al., 2003). Similarly, the accuracy of the altimetry varies with the width of the river, with accuracy improving over wider river

channels. Other limitations arise due to errors associated with the estimation of the bankfull Froude number and mean flow velocity (which are key to estimating the channel depth and flow resistance), and due to the approximation of the river channel cross-section as a parabola. Without calibration, the errors associated with the remote observations and the estimation of channel depth and cross-section shape contribute significantly to the error of the discharge estimates, although with calibration, the effects of these errors are reduced because of the inherent forcing of the calibration process. However, even with the calibration forcing, the errors and uncertainty associated with the approximation of the channel cross-section shape will affect the error in estimates of depth and velocity.

The mean accuracy of the uncalibrated discharge estimates at both Stevens Village and Eagle, as compared with the USGS measured values over the period of record, range within +/- 20% based on the mean absolute residual and +/- 10% (approximately) based on the mean of the log residual (log of the estimate minus log of the USGS measured discharge – note the mean of the log residual can be approximately interpreted as the percent error of the estimate weighted by the log transformation). This range of accuracy is within what might be expected from ground-based indirect measurements of discharge (Herschey, 1998; Dickerson, 1967). The calibrated discharge estimates showed a range of accuracy of +/- 2%, which is well within USGS standards for a fair to good ground-based measurement (Rantz et al., 1982), indicating that with appropriate calibration, the satellite based measurements of stage, slope, and reach averaged width can be used to develop discharge estimates suitable for most applications.

The bias in the uncalibrated discharge varies substantially between the two gaging stations indicating that the methods proposed in this paper, without calibration, do not provide sufficient site specificity to capture the full range of flows in each case. Additionally, the high and low end bias are not necessarily reduced by minimizing or eliminating the mean bias. The high and low bias indicates that use of a constant or narrow range of roughness is insufficient to capture the full range of flows. Scale dependent

and reach specific properties that affect flow resistance in the channel, and thus the value of the roughness coefficient, need to be accounted for if relatively accurate estimates across the full range of discharge are desired at each river reach. A fuller understanding of the nature of errors and limitations of using remote sensing observations and employing approximations to the channel cross-section and flow resistance will require a much larger number of study sites over a wide range of river sizes.

The spatial interpolation of water surface elevations measured by satellite altimetry are in good agreement with in situ gage measurement. The water surface slope spatiotemporal variability indeed reflects the energy balance along flow direction between the gravity driving the flow and energy dissipation showing it is a useful proxy for characterizing hydraulic behavior river reaches (Garambois et al., 2016). We show it is a useful proxy for characterizing hydraulic behavior of reaches under sufficient hydraulic visibility condition. Interestingly, our results show that the altimetry generated water surface slopes derived from the elevations gained by altimetry, for reaches of 41 km for Stevens and 36 km for Eagle, produce relatively accurate discharge estimations. Further investigations may be needed to assess optimal reach length for water surface slopes calculations in various hydro-morphological contexts and measurement accuracies. Additional investigations may also be needed to better understand how to predict the flow resistance and roughness height from the observable channel morphology.

The disparity between the USGS and uncalibrated estimates (particularly at Eagle) indicates the need for additional information, such as mean discharge from a hydrologic model or other source, or limited field data (for example several ADCP measurements in the reach of interest at different flow levels), to calibrate the method. Tarpanelli et al. (2015) showed that surface velocity can be estimated using reflectance properties of MODIS NIR based on a regional relation that correlates with velocity. Surface velocity in rivers may also be measured from aircraft and possibly from satellites. If surface velocity were periodically available as an additional remotely observed hydraulic variable, more accurate estimates of discharge and roughness may be possible based on methods described by Moromarco et al. (2013).

Another example is the explicit equation proposed by Garambois and Monnier (2015), which allows the derivation of accurate effective river bathymetry profiles from one river snapshot of water surface slope and width distributed in space along with one unique in situ depth estimation.

The temporal resolution of the Jason-2 overpasses prevents having any certainty of observing the maximum or true mean of the flow. This limitation also reduces the possibility of observing the full range of fluctuation in depth and velocity that might otherwise provide valuable data that could be used to minimize estimation error associated with the assumption of a regular parabolic cross-section shape. However, periodic observations do provide a time series, albeit temporally incomplete, that can be a valuable reflection of hydrologic conditions in the contributing watershed, particularly if the observations are maintained over a long period of record. However, in light of this issue, it should be noted that other altimeters currently in orbit could increase the temporal density of the observations. Also, low cost transducers could be placed in the river and retrieved periodically that can be correlated with the altimeter observations and used to fill in the temporal gaps.

The calibration of the discharge assumes a continuous function to represent the variation in Manning  $n$  values with depth, and as such does not account for possible thresholds of flow resistance due to changing control. This is especially problematic if the method were applied to overbank flood flow, at which time a dramatic change in flow resistance for the entire cross-section would be expected. Future work will necessarily need to focus on how to adjust flow resistance for the cross-section during overbank flooding conditions, presuming that the overbank flow cross-section would be known a priori from available digital elevation model (DEM) information for the floodplain.

Without remote sensing instruments that can detect surface velocity or river bathymetry, it is less likely that remote sensing information alone can be used to consistently and accurately estimate the discharge in rivers of varying morphologies and flow controls. Indeed, the method presented here, which indirectly

incorporates a significant number of in situ variables via the empirical relationships calibrated by Bjerklie (2007), remain subject to significant bias. To address this shortcoming and in the absence of an objective function that can be used for calibration, other hydraulic relations may be employed to constrain the discharge estimates. First and foremost is continuity. It is conceivable that downstream estimates of discharge can be constrained by the upstream estimates using various mathematical techniques (Durand et al., 2015; Paris et al., 2015), however there would still need to be a reference point, for example a gaging station, to assess the accuracy of the estimates. It is also possible that river regime concepts could be used to help understand the probable state of the river channel in a downstream direction. However regime theory cannot adequately address variability across different river morphologies and geologic terrain.

Another possibility for constraining the discharge estimate is to compare the meander length to the backwater length (in this case the backwater curve associated with a mild channel slope with the water surface rising to the normal depth, referred to as an M2 curve) , calculated using the estimated Froude number, as discussed in sections 2.0 and 3.0 using equation (16) (Davidian, 1984).

$$L_{bw} = (0.57-0.79 F^2) * \frac{Y}{S} \quad (16)$$

$L_{bw}$  = approximate M2 backwater length, (ft)

$S$  = water surface slope

$Y$  = mean water depth, (ft)

Fig. 19 shows the relationship between the calculated backwater length and the along channel meander length for a set of 48 rivers (data from Bjerklie 2007). The relation is sufficiently strong between the expected Froude number and the expected ratio computed from the Froude that it could be leveraged to constrain the estimated depth. The relation may also be used to help predict the flow resistance.



*Figure 19 - Ratio of backwater to resistance length as a function of Froude number for natural rivers, showing the logarithmic best fit line given by the equation shown on the chart with the associated coefficient of determination ( $r^2$ ).*

A very promising approach to integrating remote sensing and streamflow monitoring is to combine the remote observations with regional water balance models that can supply annual or monthly mean values that can be used to scale the dynamic remotely-sensed sensing observations (Paris et al., 2015), and to fill in discharge along the river network between remote sensing based gages. As part of a USGS effort to estimate streamflow in ungaged watersheds, to understand runoff quantity and timing between gaging stations, and to estimate potential future streamflow, a coarse-scale national application of the Precipitation Runoff Modeling System model (PRMS; Markstrom et al., 2015) is under development by the USGS. Once completed, it might supply sufficient information with adequate accuracy to augment and provide scale to a remote sensing-based streamflow gaging network.

Additionally, the inclusion of rapidly deployed ground-based radar instrumentation to develop discharge ratings and channel bathymetry can be used in an effective manner to define channel shape, slope, bathymetry, and velocity relations that correspond to highly accurate discharge ratings. Field and laboratory trials were conducted to demonstrate the efficacy of using ground-based continuous-wave (CW) radars and the Probability Concept (Chiu and Tung, 2002; Chiu, 1987; Fulton and Ostrowski, 2008; Fulton, 1999) to ground-truth space-based discharges. The proviso was that a site-of-interest does not require historical stage-discharge, slope-discharge, or velocity-discharge data. Radar-derived versus conventional stage-discharge ratings for the Rio Grande at Embudo, New Mexico, USA from April 2014 to September 2015 yielded a Nash-Sutcliffe Efficiency of 0.99 ( $n = 44,600$  individual discharge values

ranging from 207 cubic feet per second ( $\text{ft}^3/\text{s}$ ) to 4,140  $\text{ft}^3/\text{s}$ ). The research demonstrates that instantaneous streamflow can be computed using the Probability Concept for a range of hydraulic extremes immediately after the siting phase is complete. This is particularly important at sites where new streamgages are planned or at hydraulically complex sites, where shifts and corrections are necessary to develop and maintain stage-discharge ratings. Simply put, real-time streamflow can be computed using the Probability Concept and CW radars without the need to develop and maintain a stage-, slope, or velocity-discharge rating.

It is conceivable that temporary streamgages could be deployed at key locations in the river network and operated for a brief period, and then moved to other locations. Once defined, the channel relations (assuming stable channel conditions) can then serve as the absolute reference for the remote sensing observations, potentially yielding highly accurate discharge estimates entirely from satellite observations.

The combination of watershed modeling and limited field work may provide the basic framework for interpreting remote sensing observations such that river flow dynamics and average discharge can be evaluated with reasonable accuracy. Additionally, and possibly more importantly, the frequency of observation from satellite platforms, even when using multiple satellites to increase temporal density of observations, will not provide the needed temporal resolution for many applications, for example tracking flood waves (except on the very largest rivers). However, the remote sensing and the modeling can provide full spatial coverage for many river systems of interest, and therefore the combination of information from these tools, with limited field work and gaging locations, can essentially periodically map the river hydraulics and dynamics, pointing towards an efficient approach to understanding the river network in its entirety. Additionally and potentially most importantly, the use of archived imagery and satellite altimetry may provide a means to reconstruct past river discharge time series for rivers that do not have gages on them, or where the gages have only been in place for a short period. This possibility may be particularly important in rivers flowing to the Arctic Ocean (Bring et al., 2016).

## 5.0 Conclusions

In this study, methods for computing streamflow from remotely sensed data were tested in two reaches of the Yukon River, one inclusive of the USGS streamgage at Eagle, Alaska (station number 15356000) and one inclusive of the USGS streamgage near Stevens Village, Alaska (station number 15453500). The methods use the water surface area derived from Landsat via the dynamic surface water extent (DSWE) methodology to determine the average water surface width, and the Jason-2 radar altimeter was used to measure water surface height (stage) and slope. Additional observations from the ICESat laser altimeter also enabled a cross-validation of the Jason-2 slope estimates. The Landsat imagery and the satellite radar altimetry information showed that they could provide sufficient data to estimate the discharge and hydraulic conditions at two locations in the Yukon River with reasonable accuracy provided there is a reference discharge that can be used to calibrate the bottom height of the channel relative to the water surface stage. Two physically based flow resistance equations were used to estimate discharge, the Manning equation (MAN) and one based on the Prandtl-von Karman (PVK) universal flow velocity distribution equation. Both equations use depth and slope to estimate velocity with a flow resistance coefficient. Along with width estimated from a limited number of satellite observations correlated with the Jason-2 water heights, the discharge was then calculated. The key issues are estimating the flow resistance coefficients and defining a reference height that enables the water surface height measurements to translate to a depth. In this study we use the channel bottom elevation as the reference height, deriving its value from paired observations of width and stage, and we estimate the flow resistance from observations of channel morphology, or calibrate its value directly with a minimum of ground-based discharge measurements.

The uncalibrated discharge estimates on average, were estimated to within 20% of the USGS measured value for the each of the two study reaches. In general, the MAN equation reproduces the hydraulic

relations between discharge, depth, and velocity somewhat better than the PVK equation. However, these estimates tend to be biased, so that the error is large on the low and high ends of the flow range. The bias can be resolved by calibrating on limited discharge measurements (in this study three measurements were used) that are representative of the typical low, mid, and high flow range. Additionally, the three point calibrations show that the range in measured flow is wider than can be represented by a constant or narrow range of roughness coefficient values. This indicates that the method used to estimate the change in flow resistance with depth is an important hydraulic characteristic that needs to be accurately modeled. Once calibrated, the discharge estimates using the MAN equation may be well within typical accuracies associated with USGS streamgages that are rated fair to good ( $\pm 5\%$ ).

The capability of estimating discharge remotely from optical satellite imagery (e.g. Landsat, Sentinel-2, and various commercial systems), radar imagery (e.g. RADARSAT-2, TerraSAR-X), and existing (Cryosat-2, Sentinel-3, Jason-3) and future (ICEat-2, SWOT) altimetric missions provides an opportunity to fill in missing data and extend records at USGS gages, can be used to extend the gage network, and can potentially supplement ground-based gaging networks to create a more spatially and temporally dense set of observations around the globe. The use of satellite imagery and radar remote sensing to estimate discharge in rivers is subject to limitations regarding the size of the river that can be observed due to resolution of the imagery and radar footprint, the non-coincident observations of water surface width and height in the rivers, the orbital spacing and observation frequency, accuracy of the estimates due to the need for generalized hydraulic assumptions to set the channel bottom depth, shape and flow resistance especially if there is not ground-based calibration, and the inability to apply these data to ice-covered rivers. The issue of the non-coincidence of the width and height observations will be alleviated with the upcoming NASA SWOT mission, but the other issues will remain and will need to be addressed if future streamflow gaging networks are designed to incorporate independent satellite-based streamflow estimates. However, it is important to recognize that the satellite information can be very useful for mapping river systems and tracking flow dynamics even if it is not used to directly estimate the discharge.

The Landsat imagery and the satellite altimetry information provides sufficient data to estimate the discharge and hydraulic conditions at two locations in the Yukon River, provided reference discharges are available that can be used to calibrate the bottom height of the channel relative to the water surface stage. Based on this study, we have developed the following general conclusions regarding the use of Landsat and altimetry to estimate discharge:

- 1) Landsat and satellite altimetry can successfully track river dynamics at the two study locations in the Yukon River.
- 2) Combined with additional hydrologic information such as limited field surveys, Landsat imagery and altimetry can be used to estimate river discharge and river hydraulic conditions with reasonable accuracy.
- 3) Time series of Landsat and altimetry data can be used to develop reach scale stage-width relations, and with additional imagery, would be expected to increase the estimated accuracy of discharge, depth, and velocity. The proposed SWOT mission would provide width observations coincident with stage observations, eliminating the need to derive relations that can be applied when width is not available.
- 4) Because the discharge algorithms used in this study are physically based, they are adaptable to any new relevant information that may be available for the estimation of river hydraulics.
- 5) The combined use of remote sensing, modeling, and the gage network can conceivably provide the framework for periodically mapping the spatial characteristics of the hydraulics and dynamics of a river network at different flow levels, pointing towards an efficient method for understanding the river system in its entirety.

The capability of estimating discharge remotely in Alaska provides an opportunity to use this information to fill in missing data and extend records at USGS gages, as well as construct historical flow records for river reaches with little or no ground-based measurements, but where archived satellite observations are

available. That is, systematically collected satellite data can be used to extend records as far back as remote sensing data are available, and forward given a planned strategy to use remote sensing information in conjunction with limited field data at existing gages. Thus, remote sensing may be used to establish a more dense spatial gage network with remote sensing based gages that incorporate time series of Landsat and altimetry observations such that a time series is available at the gage even before any field data are collected. The subsequent limited field data could then calibrate the time series, providing a dynamic record that at a minimum can be compared against itself to evaluate trends. This study demonstrates that existing imagery and altimetry data will be valuable supplements to the future SWOT information to create a more temporally dense set of observations at any given location on the globe.

#### 8.0 Acknowledgements

The authors acknowledge NASA grant NNX13AH15G with respect to the radar and lidar altimetry analysis, and would like to thank J. Toby Minear, research hydrologist with the Earth Science and Observation Center (ESOC) Cooperative Institute for Research in Environmental Sciences (CIRES) at the University of Colorado, Boulder for invaluable comments during the development of this paper, and Jeff Conaway, Alaska Branch Chief of Hydrologic Investigations and Monitoring U.S. Geological Survey, for providing a thorough and incisive review of this paper.

#### 9.0 References

Abshire, J. B., X. Sun, H. Riris, J. M. Sirota, J. F. McGarry, S. Palm, D. Yi, and P. Liiva, 2005, Geoscience Laser Altimeter System (GLAS) on the ICESat Mission: On-orbit measurement performance, *Geophys. Res. Lett.*, 32, L21S02, doi:10.1029/2005GL024028.

Alsdorf, D., Birkett, C.M., Dunne, T., Melack, J., and Hess, L., 2001. Water level changes in a large Amazon lake measured with spaceborne radar interferometry and altimetry, *Geophysical Research Letters*, 28 (14), pp. 2671–2674.

Alsdorf, D., D. Lettenmaier, and C. Vörösmarty, 2003, The need for global, satellite-based observations of terrestrial surface waters, *Eos Trans. AGU*, 84(29), pp. 269–276, doi:[10.1029/2003EO290001](https://doi.org/10.1029/2003EO290001).

Alsdorf, D. E., E. Rodríguez, and D. P. Lettenmaier, 2007, Measuring surface water from space, *Rev. Geophys.*, 45, RG2002, doi:[10.1029/2006RG000197](https://doi.org/10.1029/2006RG000197).

AVISO, <http://www.aviso.altimetry.fr/en/data/tools/pass-locator.html>, 2016.

Barnes, H.H., 1967. Roughness characteristics of natural channels, USGS Water-Supply Paper 1849, 213p.

Birkett, C.M., 1995. The contribution of TOPEX/POSEIDON to the global monitoring of climatically sensitive lakes, *JGR-Oceans*, 100, C12, pp.25, 179-25, 204.

Birkett, C.M., 1998. Contribution of the TOPEX NASA radar altimeter to the global monitoring of large rivers and wetlands. *Water Resources Research* 34 (5), pp. 1223–1239.

Birkett, C. M., L. A. K. Mertes, T. Dunne, M. H. Costa, and M. J. Jasinski, 2002. Surface water dynamics in the Amazon Basin: Application of satellite radar altimetry, *J. Geophys. Res.*, 107(D20), 8059, doi:[10.1029/2001JD000609](https://doi.org/10.1029/2001JD000609)

Birkett, C.M., D. Alsdorf, and D. Harding, 2005. Estimation of River and Water Body stage, width and gradients using Radar Altimetry, Interferometric SAR and Laser Altimetry, Volume 2 Part 5 (Remote Sensing) chapter 60, in *The Encyclopedia of Hydrological Sciences*, ed. M.G. Anderson, John Wiley & Sons Ltd. Chichester, UK., ISBN: 978-0-471-49103-3.

Birkett, C.M. and B. Beckley, 2010. Investigating the Performance of the Jason-2/OSTM radar altimeter over Lakes and Reservoirs, *Jason-2/OSTM Special Issue, Marine Geodesy*, 33(1), pp.204-238.

Birkett, C.M., D.M. Bjerklie, M. Hofton, Y. Li, R. Dubayah, 2010, Application of ICESat/GLAS laser altimetry to the estimation of Surface Water Level and River Discharge, presented at the 2010 Fall Meeting, AGU, San Francisco, Calif., 13-17 Dec., Abstract C43F-02.

Birkinshaw, S.J., G.M. O'Donnell, P. Moore, C.G. Kilsby, H.J. Fowler, P.A.M. Berry, 2010. Using satellite altimetry data to augment flow estimation techniques on the Mekong River. *Hydrological Processes* 24(26), pp. 3811–3825. doi:10.1002/hyp.7811

Birkinshaw, S.J., P. Moore, C.G. Kilsby, G.M. O'Donnell, A.J. Hardy, P.A.M. Berry, 2014. Daily discharge estimation at ungauged river sites using remote sensing. *Hydrological Processes* 28(3), pp. 1043–1054. doi:10.1002/hyp.9647

Bjerklie, D.M., 2007. Estimating the bankfull velocity and discharge for rivers using remotely sensed river morphology information, *Journal of Hydrology* 341 (3-4), pp. 144-155.

Bjerklie, D.M., D. Moller, L.C. Smith and S.L. Dingman, 2005. Estimating discharge in rivers using remotely sensed hydraulic information, *Journal of Hydrology*, 309, pp. 191-209.



Bjerklie, D.M., Lawrence Dingman, S., Vörösmarty, Charles J., Bolster, Carl H., Congalton, Russell G., 2003. Evaluating the potential for measuring river discharge from space. *Journal of Hydrology* 278 (1–4), pp. 17–38.

Bonnema, M. G., S. Sikder, F. Hossain, M. Durand, C. J. Gleason, and D. M. Bjerklie, 2016. Benchmarking wide swath altimetry-based river discharge estimation algorithms for the Ganges river system, *Water Resour. Res.*, 52, pp. 2439–2461, doi:[10.1002/2015WR017296](https://doi.org/10.1002/2015WR017296).

Boy, J.-P., and C.C. Carabajal, 2013. Lake and reservoir water level measurements from ICESat laser altimetry. *Proc. 20 Years of Progress in Radar Altimetry*, Venice, Italy, 24–29 September 2012, ESA SP-710.

Brabets, Timothy P., Bronwen Wang, and Robert H. Meade, 1999. Environmental and Hydrologic Overview of the Yukon River Basin, Alaska and Canada, U.S. Geological Survey Water-Resources Investigations Report 99-4204, 106 p.

Brakenridge, G.R., S. V. Nghiem, E. Anderson, and R. Mic, 2007. Orbital microwave measurement of river discharge and ice status, *Water Resour. Res.*, 43, W04405 doi:[10.1029/2006WR005238](https://doi.org/10.1029/2006WR005238).

Bring, A., A. Shiklomanov, and R. B. Lammers, 2016. Pan-Arctic river discharge: Prioritizing monitoring of future climate change hot spots, *Earth's Future*, 5, doi:[10.1002/2016EF000434](https://doi.org/10.1002/2016EF000434).

Calmant, S., F. Seyler, A. Cazenave and F. Frappart, 2004. Amazon River Stages by ENVISAT vs. Other Satellite Altimeters, Poster Session 4P12-02 “Lake Levels”, Abstract 671, 2004 ERS and ENVISAT Symposium, Salzburg, September.

Camporeale, C., Perona, P., Proporato, A., Ridolfi, L., 2005. On the long-term behavior of meandering rivers. *Water Resources Research* 41, W12403 doi:10.1029/2005WR004109.

Canova, M.G., Fulton, J.W., and Bjerklie, D.M., 2016, USGS HYDRoacoustic dataset in support of the Surface Water Oceanographic Topography satellite mission (HYDRoSWOT): U.S. Geological Survey data release, <http://dx.doi.org/10.5066/F7D798H6>.

Carabajal, C.C., J-P Boy, S.B. Luthcke, D.J. Harding, D.D. Rowlands, F.G. Lemoine, and D.S. Chin, 2006. Recovery of the Three-Gorges reservoir impoundment signal from ICESat altimetry and GRACE, *Eos Trans. AGU*, **87**(52), Fall Meet. Suppl., Abstract G13C-06.

Carroll, M., M. Wooten, C. DiMiceli, R. Sohlberg, and M. Kelly, 2016. Quantifying surface water dynamics at 30 meter Spatial resolution in the North American high northern latitudes 1991–2011. *Remote Sensing*, 8 (8) 622, doi:10.3390/rs8080622 .

Chiu, C.-L., and Tung, N.C., 2002. Velocity and regularities in open-channel flow. *Journal of Hydraulic Engineering*, 128(4), pp. 390-398.

Chiu C-L., 1987. Entropy and probability concepts in hydraulics. *Journal of Hydraulic Engineering*, 113(5), pp. 583–600.

Chow, Ven Te, 1959. *Open-Channel Hydraulics*, McGraw-Hill Civil Engineering Series, New York, p. 680.

Church, M., Rood, K., 1983. Catalogue of alluvial river channel regime data, first ed. Department of Geography, University of British Columbia, Vancouver, Canada.

Clement, David T., 1999. Fluvial Geomorphology of the Yukon River, Yukon Flats, Alaska, A Thesis submitted to the faculty of graduate studies in partial fulfillment of the requirements for the degree of Master of Science, Department of Geography, University of Calgary, Calgary, Alberta, p. 199.

Coon, W.F., 1998. Estimation of roughness coefficients for natural stream channels with vegetated banks. U.S. Geological Survey Water- Supply Paper 2441. p. 133.

Davidian, Jacob, 1984. Computation of water-surface profiles in open channels, Techniques of Water-Resources Investigations of the United States Geological Survey, Applications of Hydraulics Book 3, Chapter A15, p. 57.

Dickerson, W.T., 1967. Accuracy of discharge determinations, Hydrology Papers, Colorado State University, Fort Collins Colorado, p. 20.

Dingman, S.L., Palaia, K., 1999. Comparison of models for estimating flood quantiles in New Hampshire and Vermont Journal of the American Water Resources Association 35, 1233–1243.

Dingman, S.L. and D.M. Bjerklie, 2006. Hydrological Application of Remote Sensing: Surface Fluxes and other Derived Variables-River Discharge, in *Encyclopedia of Hydrological Sciences*. John Wiley and Sons, pp. 5–61. doi:10.1002/0470848944.

Dingman, S. Lawrence, 2007. Analytical derivation of at-a-station hydraulic-geometry relations, Journal of Hydrology, 334, pp. 17-27.

Dingman, S. Lawrence, 2009, *Fluvial Hydraulics*, Oxford University Press, p. 559.

Durand, M., J. Neal, E. Rodríguez, K.M. Andreadis, L.C. Smith LC, and Y. Yoon, 2014. Estimating reach-averaged discharge for the River Severn from measurements of river water surface elevation and slope. *Journal of Hydrology* 511(C), pp. 92–104. doi:10.1016/j.jhydrol.2013.12.050

Durand, M., C. J. Gleason, P. A. Garambois, D. Bjerklie, L. C. Smith, H. Roux, E. Rodriguez, P. D. Bates, T. M. Pavelsky, J. Monnier, X. Chen, G. Di Baldassarre, J.-M. Fiset, N. Flipo, R. P. d. M. Frasson, J. Fulton, N. Goutal, F. Hossain, E. Humphries, J. T. Minear, M. M. Mukolwe, J. C. Neal, S. Ricci, B. F. Sanders, G. Schumann, J. E. Schubert, and L. Vilmin, 2016. An intercomparison of remote sensing river discharge estimation algorithms from measurements of river height, width, and slope, *Water Resour. Res.*, 52, pp. 4527–4549, doi:[10.1002/2015WR018434](https://doi.org/10.1002/2015WR018434).

Fekete, Balazs and Charles J. Vörösmarty, 2007. The current status of global river discharge monitoring and potential new technologies complementing traditional discharge measurements, Predictions in Ungauged Basins: PUB Kick-off (Proceedings of the PUB Kick-off meeting held in Brasilia, 20-22 November, IAHS Publ. 309.

Ferguson, R. (2007), Flow resistance equations for gravel- and boulder-bed streams, *Water Resour. Res.*, 43, W05427, doi:[10.1029/2006WR005422](https://doi.org/10.1029/2006WR005422).

Fu, L.-L., and A. Cazenave, 2001. Editors. *Satellite Altimetry and Earth Sciences: A Handbook of Techniques and Applications*, Academic Press, San Diego, p. 463.

Fulton, J.W., J. Ostrowski, 2008. Measuring real-time streamflow using emerging technologies: Radar, hydroacoustics, and the probability concept. *Journal of Hydrology* 357, pp.1– 10.

Fulton, J.W., 1999. Comparison of conventional and probability-based modeling of open-channel flow in the Allegheny River, Pennsylvania, USA. Unpublished Thesis, University of Pittsburgh, Department of Civil and Environmental Engineering.

Garambois, Pierre-Andre and Jerome Monnier, 2015. Inference of effective river properties from remotely sensed observations of water surface, *Advances in Water Resources*, 79, pp. 103–120.

Garambois, P-A, S. Calmant, H. Roux, A. Paris, Monnier, J, P. Finaud-Guyot, A. Montazem, and J.S. da Silva, JS, 2016. Hydraulic visibility: using satellite altimetry to parameterize a hydraulic model of an ungauged reach of a braided river. *Hydrol. Process.*, *doi: 10.1002/hyp.11033*.

Getirana ACV, C. Peters-Lidard, 2013. Estimating water discharge from large radar altimetry datasets. *Hydrology and Earth System Sciences* 17(3), pp. 923–933. *doi:10.5194/hess-17-923-2013*.

Getirana, A.C.V., M.P. Bonnet, S. Calmant, H. Roux, O.C.R. Filho, and W.J. Mansur, 2009. Hydrological monitoring of poorly gauged basins based on rainfall–runoff modeling and spatial altimetry. *Journal of Hydrology* 379(3-4), pp. 205–219. *doi:10.1016/j.jhydrol.2009.09.049*.

Gleason C.J., L.C. Smith, 2014. Toward global mapping of river discharge using satellite images and at-many-stations hydraulic geometry. *Proceedings of the National Academy of Sciences* 111(13). *doi:10.1073/pnas.1317606111*

Grant, Gordon, 1997, Critical flow constraints flow hydraulics in mobile-bed streams: A new hypothesis, Water Resources Research, vol. 33, no. 2 pp. 349-358.

Harding, D.L and M.F. Jasinski, 2004. ICESat Observations of Inland Surface Water Stage, Slope, and Extent: A New Method for Hydrological Monitoring, Abstract: C21B-05, Fall AGU, December.

Harding, D. J., and C. C. Carabajal, 2005, ICESat waveform measurements of within-footprint topographic relief and vegetation vertical structure, Geophys. Res. Lett., 32, L21S10, doi:10.1029/2005GL023471.

Herschey, R.W., 1998. Flow measurement. In: Herschey, (Ed.), *Hydrometry: Principles and Practices*, Second ed., Wiley, Chichester, pp. 9–83.

Hicks, D.M. and P.D. Mason, 1991. *Roughness Characteristics of New Zealand Rivers*. New Zealand DSIR Marine and Freshwater Resources Survey, Wellington, NZ. p. 329.

Jarrett, R.D., 1984. Hydraulics of high gradient streams. ASCE Journal of Hydraulic Engineering 110, pp. 1519 - 1539.

Jones, J.W., 2015. Efficient wetland surface water detection and monitoring via Landsat: Comparison with in situ data from the Everglades Depth Estimation Network. Remote Sensing. Vol 7, issue 9, 12503-12538. . DOI: <http://dx.doi.org/10.3390/rs70912503>.

Kim, J-W, Z. Lu, J.W. Jones, C.K. Shum, H. Lee and Y. Jia,, 2014. Monitoring Everglades freshwater marsh water level using L-band synthetic aperture radar backscatter. Remote Sensing of Environment. B. 150, pp. 66-81

Kouraev, A.V., E.A. Zakharova, O. Samain, N.M. Mognard, and A. Cazenave, 2004. Ob' river discharge from TOPEX/Poseidon satellite altimetry (1992–2002). *Remote Sensing of Environment* 93(1-2), pp. 238–245. doi:10.1016/j.rse.2004.07.007

LeFavour, Gina, and Alsdorf, Doug, 2005. Water slope and discharge in the Amazon River estimated using the shuttle radar topography mission digital elevation model *Geophysical Research Letters*, 32, L17404, doi:10.1029/2005GL023836.

Leon, J.G., S. Calmant, F. Seyler, M.P. Bonnet, M. Cauhope, and F. Frappart, 2006. Rating curves and estimation of average water depth at the upper Negro River based on satellite altimeter data and modeled discharges. *Journal of Hydrology* 328(3-4), pp. 481–496. doi:10.1016/j.jhydrol.2005.12.006

Limerinos, J.T., 1970. Measured bed roughness in natural channels, U.S. Geological Survey Water Supply Paper 1898-B, p. 47.

Markstrom, S.L., Regan, R.S., Hay, L.E., Viger, R.J., Webb, R.M.T., Payn, R.A., and LaFontaine, J.H., 2015. PRMS-IV, the precipitation-runoff modeling system, version 4: U.S. Geological Survey Techniques and Methods, book 6, chap. B7, p. 158, <http://dx.doi.org/10.3133/tm6B7>

Moody, John A., and Brent M. Troutman, 2002. Characterization of the spatial variability of channel morphology, *Earth Surf. Process. Landforms*, 27, pp. 1251–1266.

Moramarco, T., G. Corato, F. Melone, and V. P. Singh, 2013. An entropy-based method for determining the flow depth distribution in natural channels, *Journal of Hydrology*, 497, pp. 176–188.

Osterkamp, W.R., Hedman, E.R., 1982. Perennial-streamflow characteristics related to channel geometry and sediment in Missouri River Basin, USGS Professional Paper 1242, p. 37.

Paiva, R. C. D., D. C. Buarque, W. Colischonn, M.-P. Bonnet, F. Frappart, S. Calmant, and C. A. B., Mendes, 2013. Large-scale hydrological and hydrodynamics modelling of the Amazon River basin, *Water Resources Research* 49(3):1226-1243. doi:10.1002/wrcr.20067.

Papa, F., S. K. Bala, R. Kumar Pandey, F. Durand, A. Rahman, and W. B. Rossow, 2012. “Ganga-Brahmaputra river discharge *Geophysical Research* 117: C11021. doi:10.1029/2012JC008158.

Paris, A., R. Dias de Paiva, J. Santos da Silva, D. Medeiros Moreira, S. Calmant, P.-A. Garambois, W. Collischonn, M.-P. Bonnet, and F. Seyler, 2016., Stage-discharge rating curves based on satellite altimetry and modeled discharge in the Amazon basin, *Water Resour. Res.*, 52, pp. 3787–3814, doi:[10.1002/2014WR016618](https://doi.org/10.1002/2014WR016618).

Pavelsky, T.M., 2014. Using width-based rating curves from spatially discontinuous satellite imagery to monitor river discharge. *Hydrological Processes* 28(6), pp. 3035-3040. doi:10.1002/hyp.10157.

Rantz, S.E. and others, 1982. Measurement and computation of streamflow: Volume 1 measurement of stage and discharge. U.S. Geological Survey Water Supply Paper 2175. p. 284.

Romeiser, R., J. Sprenger, D. Stammer, H. Runge, and S. Suchandt, 2005. Global current measurements in rivers by Spaceborne Along-Track InSAR, *IEEE Trans*, 0-7803-9050-4/05, pp.71-74.

Rover, Jennifer, Lei Ji, Bruce K. Wylie, and Larry L. Tieszen, 2012. Establishing water body areal extent trends in interior Alaska from multi-temporal Landsat data, *Remote Sensing Letters*, 3:7, pp. 595-604.



Schumm, S.A., 1960. The shape of alluvial channels in relation to sediment type, USGS Professional Paper 352-B.

Shiklomanov, A. I., R.B. Lammers, and C.J. Vörösmarty, 2002. Widespread decline in hydrological monitoring threatens Pan-Arctic research, *Eos Trans.,AGU*,83, pp. 13–16.

Smith, L.C., Isacks, B.L., Bloom, A.L., Murray, A.B., 1996, Estimation of discharge from three braided rivers using synthetic aperture radar satellite imagery. *Water Resour. Res.* 32 (7), pp. 2021–2034.

Smith, L. C., 1997. Satellite remote sensing of river inundation area, stage, and discharge: a review. *Hydrological Processes* 11, pp. 1427 -1439.

Spinhirne, J. D., S. P. Palm, W. D. Hart, D. L. Hlavka, and E. J. Welton, 2005, Cloud and aerosol measurements from GLAS: Overview and initial results, *Geophys. Res. Lett.*, 32, L22S03, doi:10.1029/2005GL023507.

Srivastava, P., R. Bhambri, P. Kawishwar, and D.P. Dobhal, 2013. Water level changes of high latitude lakes in Himalaya-Karakoram from ICESat altimetry, *J. Earth System Science*, 122(6), pp. 1533-1543.

Sun, X., J.B. Abshire, A.A. Borsa, H.A. Fricker, D. Yi, J.P. DiMarzio, F.S. Paolo, K.M. Brunt, D.J. Harding, G.A. Neumann (2017), ICESat/GLAS Altimetry Measurements: Signal Dynamic Range and Saturation Correction, *Transactions on Geoscience and Remote Sensing* (In Press).

Tarpanelli, A., L. Brocca, S. Barbetta, M. Faruolo, T. Lacava, and T. Moramarco, 2015. Coupling MODIS and radar altimetry data for discharge estimation in poorly gauged river basins. *IEEE Journal of*

Selected Topics in Applied Earth Observations and Remote Sensing 8(1), pp. 141-148.

doi:10.1109/JSTARS.2014.2320582.

Tulbure, M.G., and M. Broich, 2013, Spatiotemporal dynamic of surface water bodies using Landsat time-series data from 1999 to 2011. Dryad Digital Repository. ISPRS Journal of Photogrammetry and Remote Sensing 79: 44-52. <https://doi.org/10.1016/j.isprsjprs.2013.01.010>.

Vörösmarty, C.J., P. Green, J. Salisbury, and R.B. Lammers, 2000. Global water resources: Vulnerability from climate change and population growth, *Science*, 289, pp. 284–288.

Walvoord, M.A. and R.G. Striegl, 2007. Increased groundwater to stream discharge from permafrost thawing in the Yukon River basin: Potential impacts on lateral export of carbon and nitrogen, *Geophys. Res. Lett.* 34(L12402), doi:10.1029/2007GL030215.

Wang, X., P. Gong, Y. Zhao, Y. Xu, X. Cheng, Z. Niu, Z. Luo, H. Huang, F. Sun, and X. Li, 2013. Water-level changes in China's large lakes determined from ICESat/GLAS data; *Remote Sensing of Environment* 132, pp. 131-144.

Zhang, G., H. Xie, S. Kang, D. Yi, and S.F. Ackley, 2011. Monitoring lake level changes on the Tibetan Plateau using ICESat altimetry data (2003–2009), *Remote Sensing of Environment*, 115, pp. 1733–1742.

Zhu, Z, C. E. Woodcock, 2012, Object-based Cloud and Cloud Shadow Detection in Landsat TM/ETM+ images. *Remote Sensing of Environment* 118, pp. 83–94. doi: 10.1016/j.rse.2011.10.028

Zwally, H.J., B. Schutz, W. Abdalati, J. Abshire, C. Bentley, A. Brenner, J. Bufton, J. Dezio, D. Hancock, D. Harding, T. Herring, B. Minster, K. Quinn, S. Palm, J. Spinirne. and R. Thomas, 2002. ICESat's laser measurements of polar ice, atmosphere, ocean, and land. *Journal of Geodynamics*, 34 (3-4), pp.405–445.

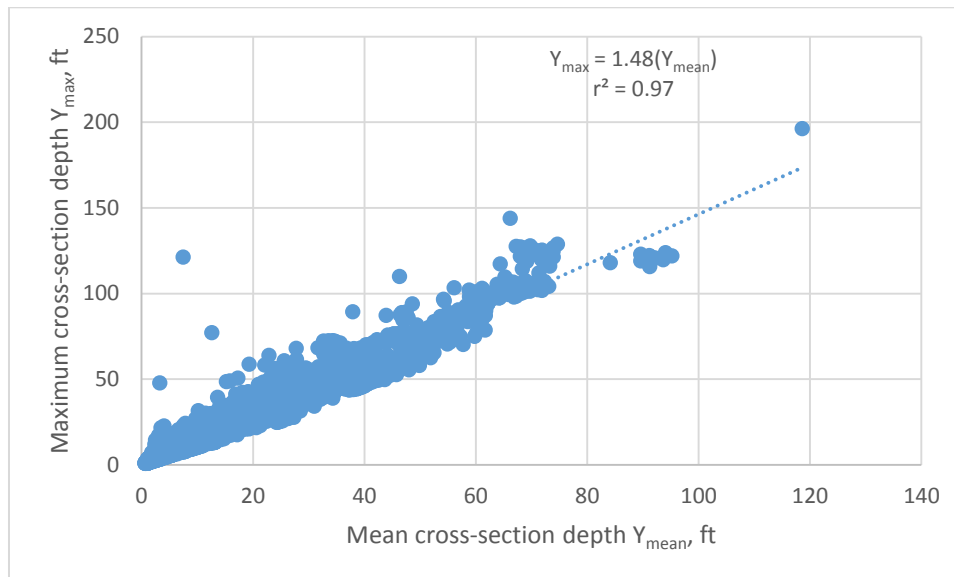


Figure 1 – Plot of the maximum depth of flow in a cross-section versus the mean depth of flow for 26,228 measured river channel cross-sections in the United States, showing a trend line with a slope of nearly 1.5, which would be the value if the general cross-section shape reflects the characteristics of a parabola. The dotted line represents the best fit line given by the equation shown on the chart with the associated coefficient of determination ( $r^2$ ).

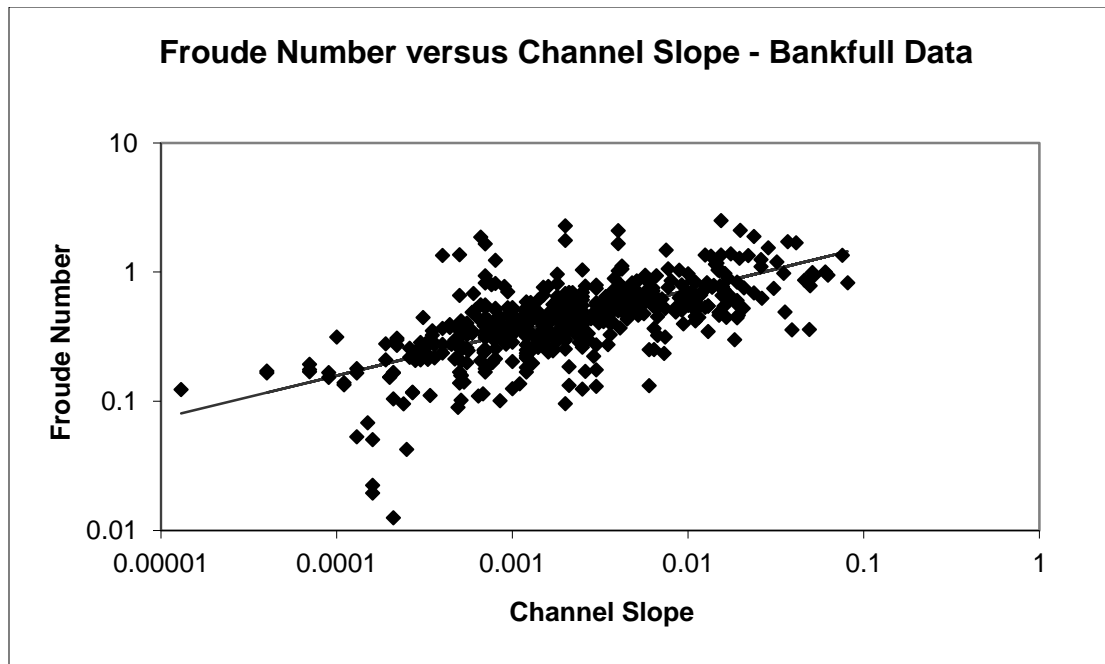


Figure 2 - Relation between  $F_b$  and slope (data from Bjerklie, 2007;  $N = 521$ , assembled from Barnes, 1967; Church and Rood, 1983; Dingman and Palaia, 1999; Osterkamp and Hedman, 1982 and Schumm, 1960, that includes rivers in the United States, Canada, and the United Kingdom). The line is the best fit given by equation (9), with a coefficient of determination ( $r^2$ ) of 0.42

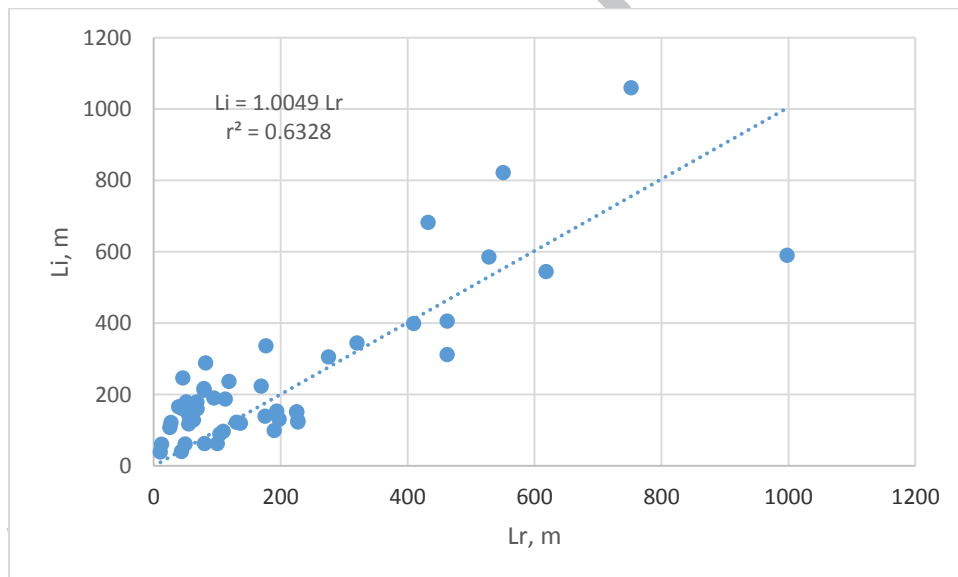


Figure 3 – Plot showing the comparison between the resistance length,  $L_r$  (Bjerklie, 2007) and the integral length,  $L_i$  (Moody and Troutman, 2002). The dotted line represents the best fit line given by the equation shown on the chart with the associated coefficient of determination ( $r^2$ ).



Figure 4 – Jason-2 (white pushpins) and ICESat (yellow pushpins) satellite crossing locations on the Yukon River reach near Stevens Village, Alaska. Jason-2 pass227 crosses both upstream (j.pass.227.1) and downstream (j.pass.227.2) of the USGS streamgauge site near Stevens Village (latitude 65.87 deg. W, longitude 149.72 deg. N marked by red circle.) ICESat pass 0342 (upstream), and passes 0223 and 0334 (downstream), are utilized in the study.

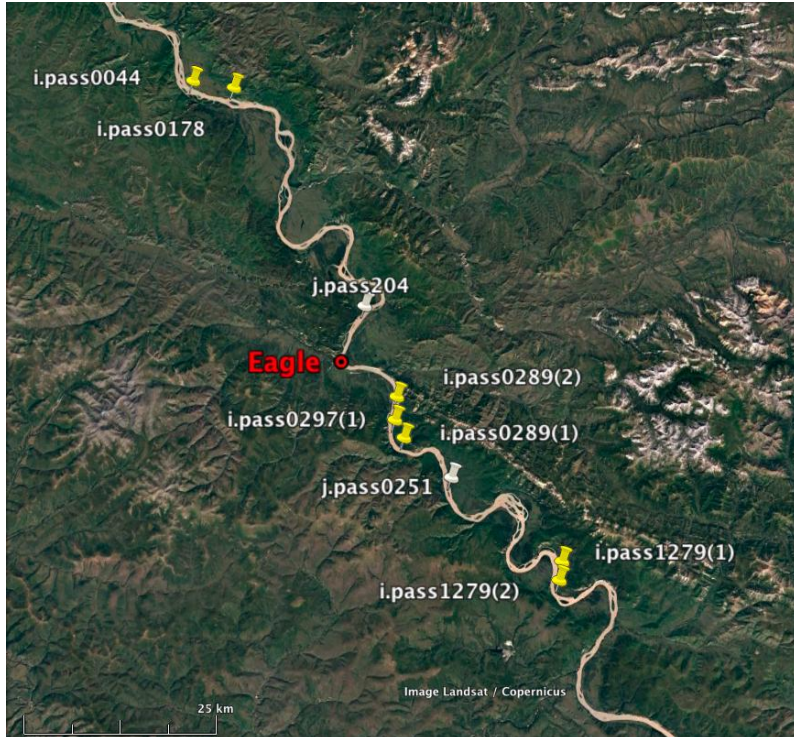
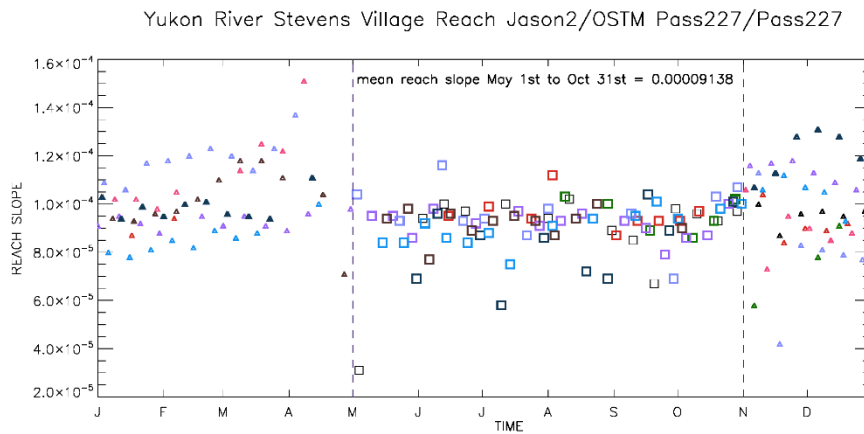


Figure 5 - Jason-2 (white pins) and ICESat (yellow pins) satellite crossing locations on the Yukon River reach at Eagle, Alaska. Jason-2 pass 251 and ICESat passes 0297 and 1279 are upstream of the USGS gauge site at Eagle (latitude 64.79 deg. W, longitude 141.2 deg. N marked by red circle). Jason-2 pass204 and ICESat passes 0044 and 0178 are downstream crossings. Due to overpass orientations and river meandering, ICESat pass 0289 strikes the river at five different locations but valid heights were only found on the upstream reach.



*Figure 6 – Seasonal Jason-2 water surface slopes Yukon River near Stevens Village, Alaska, for the reach between the upstream and downstream river crossings for pass227 over the eight year observation period – each color symbol represents a different year. Winter (November to April) slope estimates (small triangles) with greater scatter due to snow/ice penetration effects, are distinguished from those derived during the late spring through fall period (squares). The limited multi-year ICESat winter water surface slopes (green asterisks) which should not suffer from ice/snow penetration effects, are biased ~14% higher than the mean summer slope observed by Jason-2.*

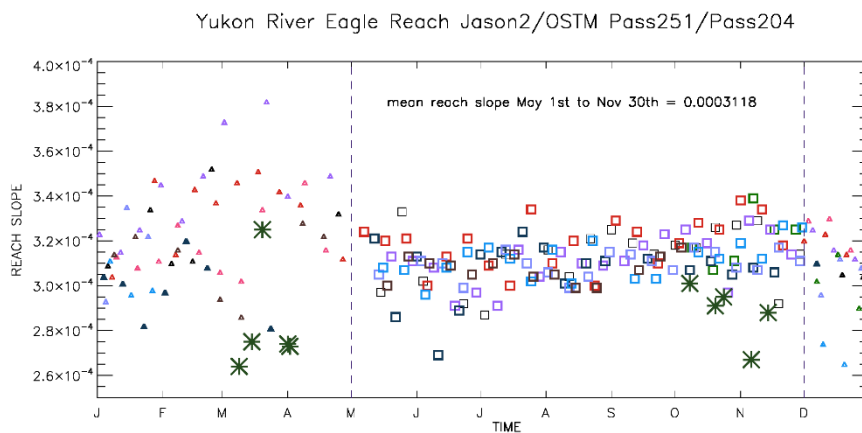


Figure 7 – Seasonal Jason-2 water surface slopes Yukon River at Eagle, Alaska, for the reach between the upstream and downstream river crossings (Pass 251 and Pass 204) over the eight year observation period – each color symbol represents a different year. Because of potential ice/snow penetration, slope estimates during a slightly shorter (December through April) winter season (small triangles) are rejected when estimating a mean reach slope value. Biased ~7% lower than this mean is the average of the multi-year multi-season ICESat water surface slopes (green asterisks) which should not be affected by snow/ice penetration.



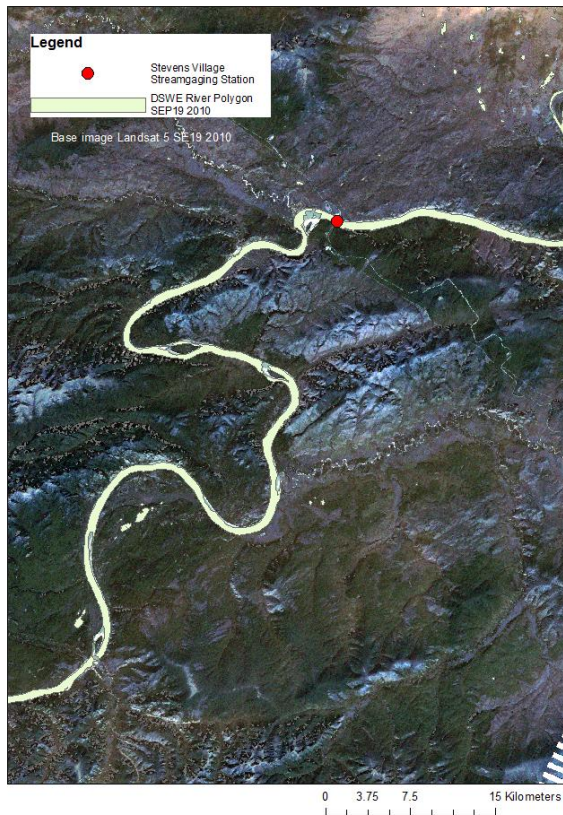


Figure 8 – Landsat image of the Yukon River near Stevens Village, Alaska, showing the Stevens Village streamgaging station (red circle, latitude 65.87 deg. W, longitude 149.72 deg.) and the water surface extent in the river channel determined from DSWE in blue-green. The flow direction is to the left.



Figure 9 – Landsat image of the Yukon River at Eagle, Alaska, showing the Eagle streamgauge (red circle, latitude 64.79 deg. W, longitude 141.2 deg.) and the water surface extent in the river channel determined from DSWE in pink. The flow direction is towards the top of the image.

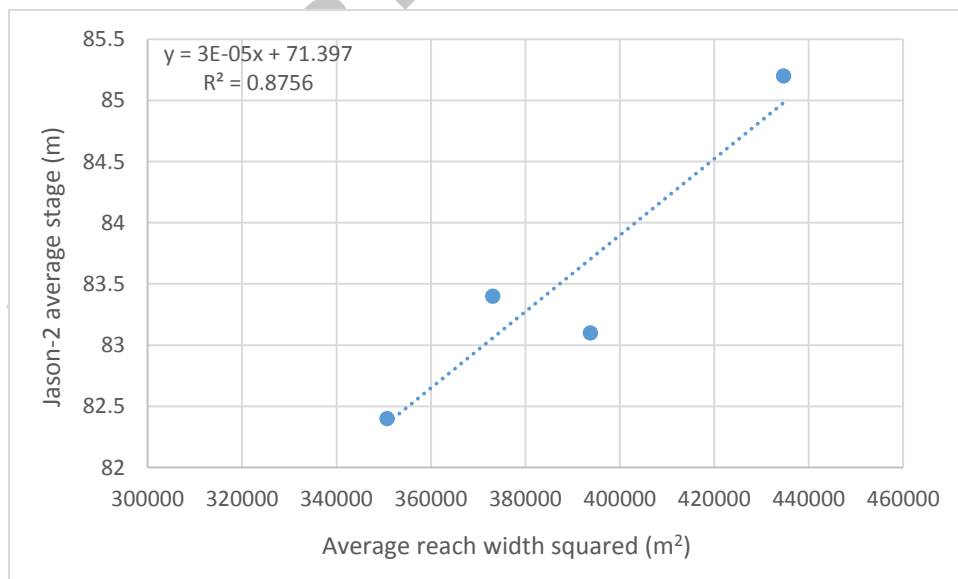


Figure 10 – Relation between Jason-2 average of the upstream and downstream observed stage and squared value of the average reach width for the Yukon River near Stevens Village, Alaska. The dotted line represents the best fit line given by the equation shown on the chart with the associated coefficient of determination ( $r^2$ ).

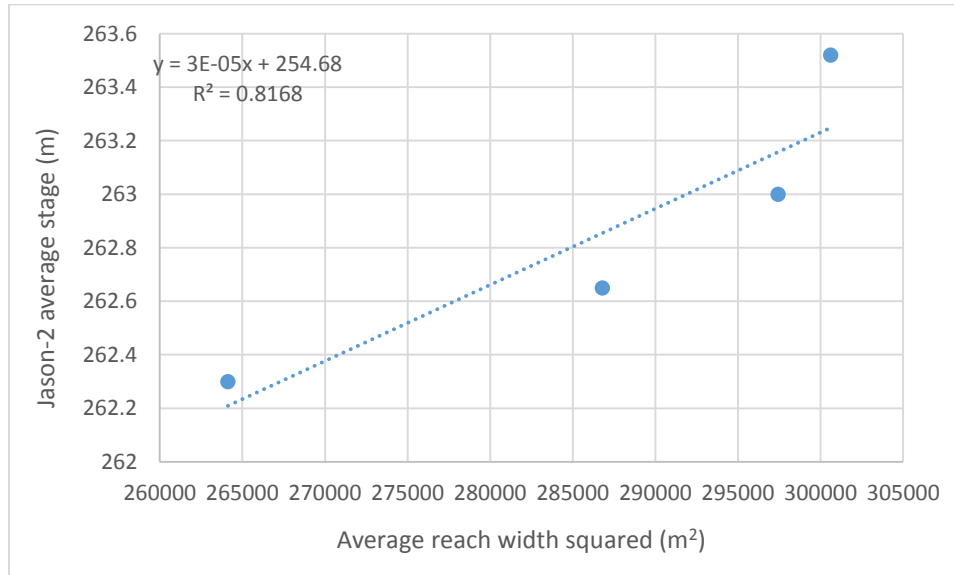
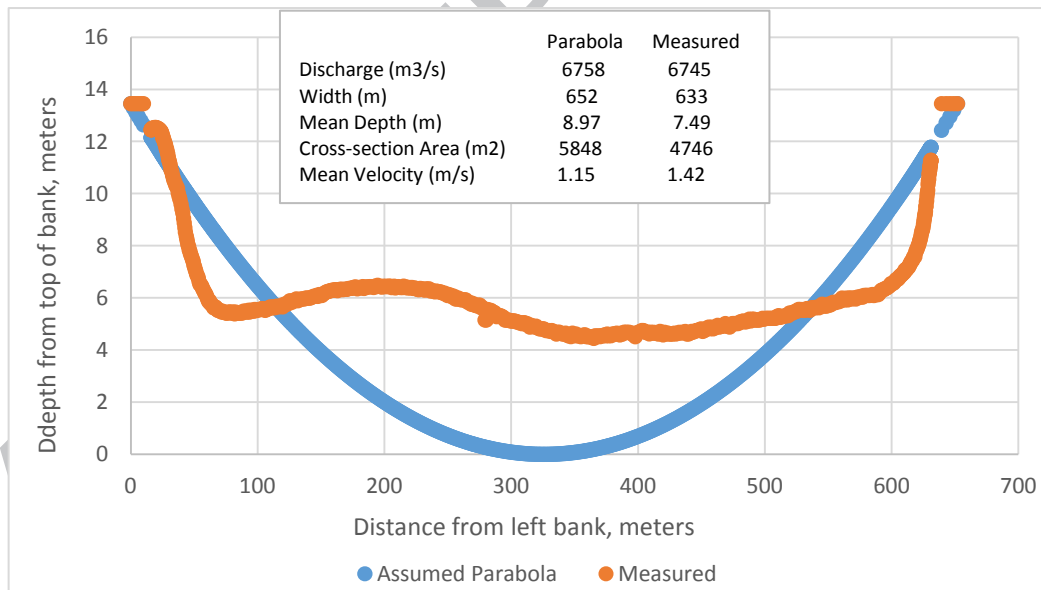
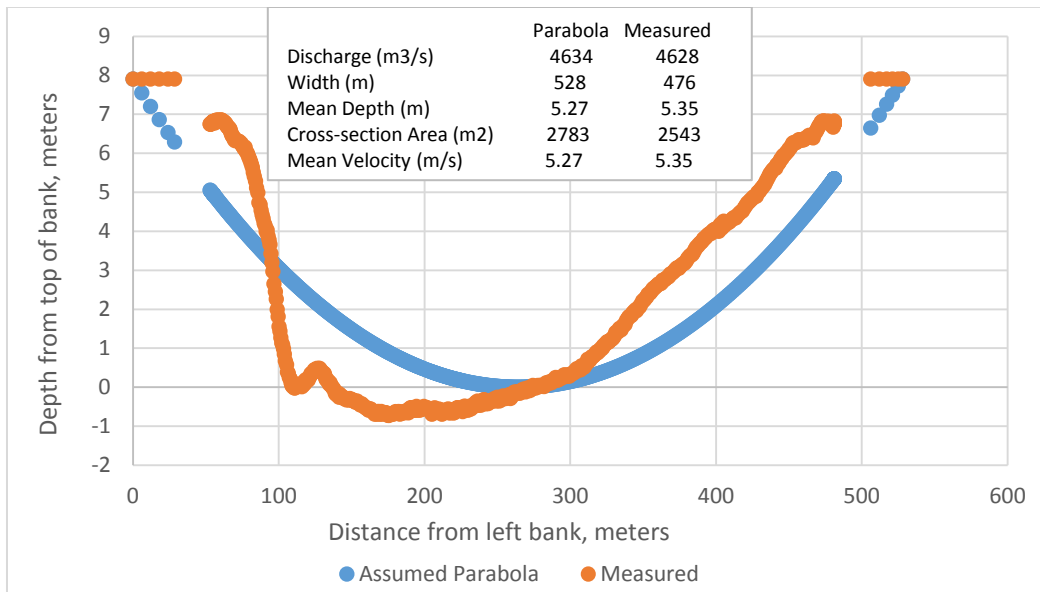


Figure 11 – Relation between Jason-2 average of the upstream and downstream observed and interpolated stage and the squared value of the average reach width for the Yukon River at Eagle, Alaska. The dotted line represents the best fit line given by the equation shown on the chart with the associated coefficient of determination ( $r^2$ ).

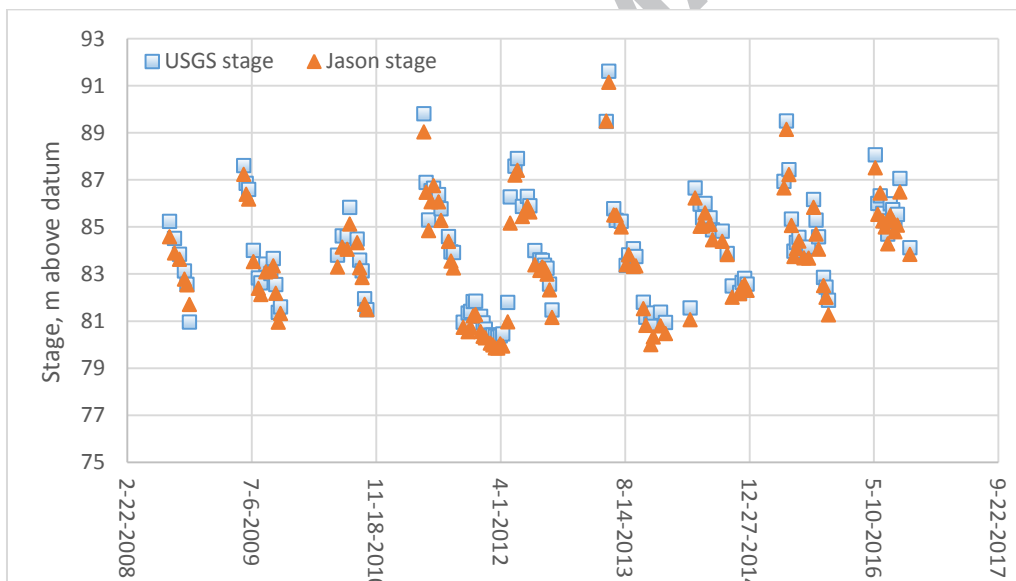


A

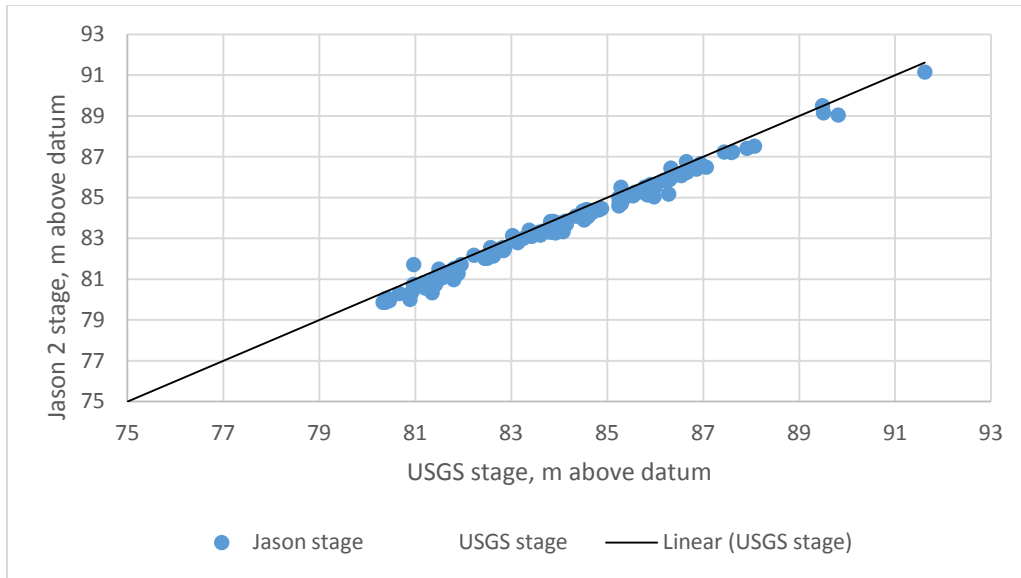


**B**

Figure 12 – Comparison between the cross-section shape and cross-section statistics for measured by the USGS at the Stevens Village (A) and Eagle (B) streamgages and the cross-section that is derived from the assumed parabolic cross-section shape for a given similar discharge.



**A**



B

Figure 13 – Average Jason-2 (average of upstream and downstream) and USGS river heights for the Yukon River reach near Stevens Village, Alaska, over (A) the 8 year period and (B) showing the linear one-to-one line.

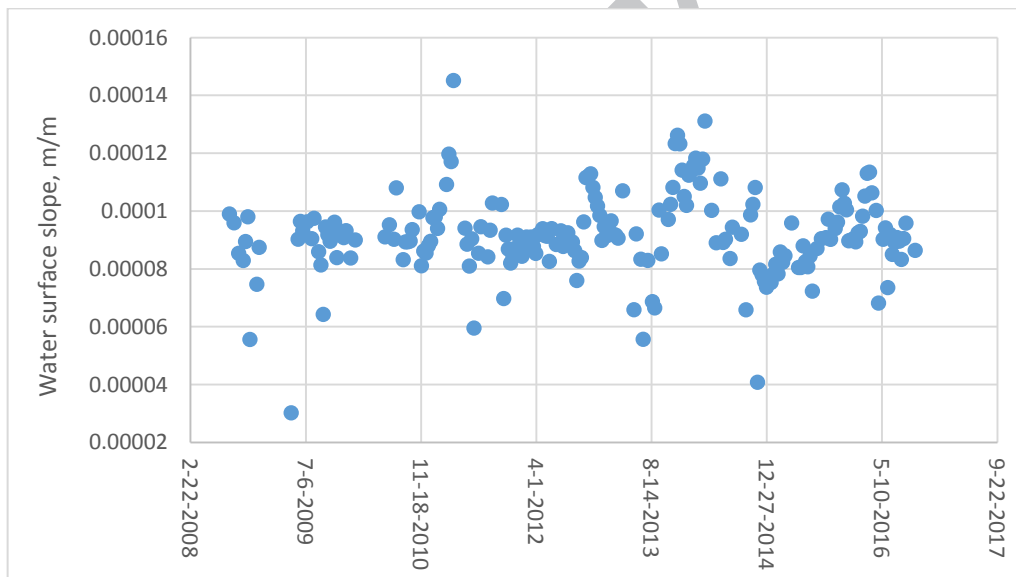
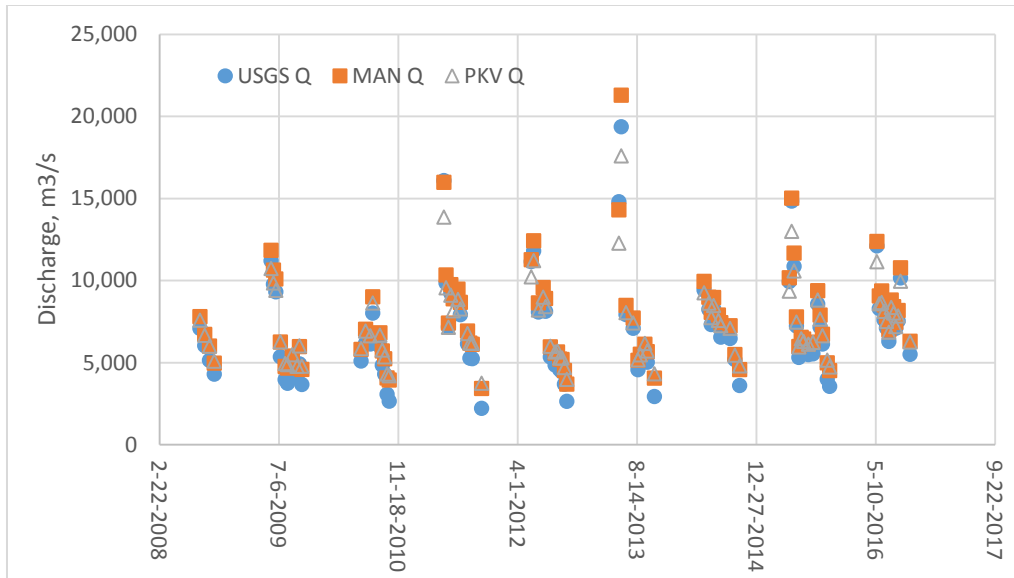
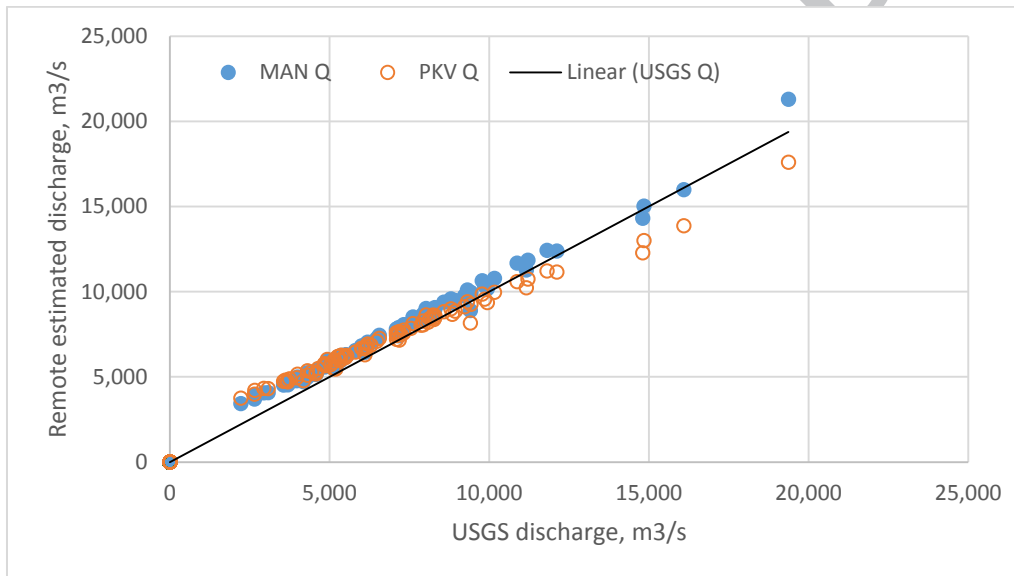


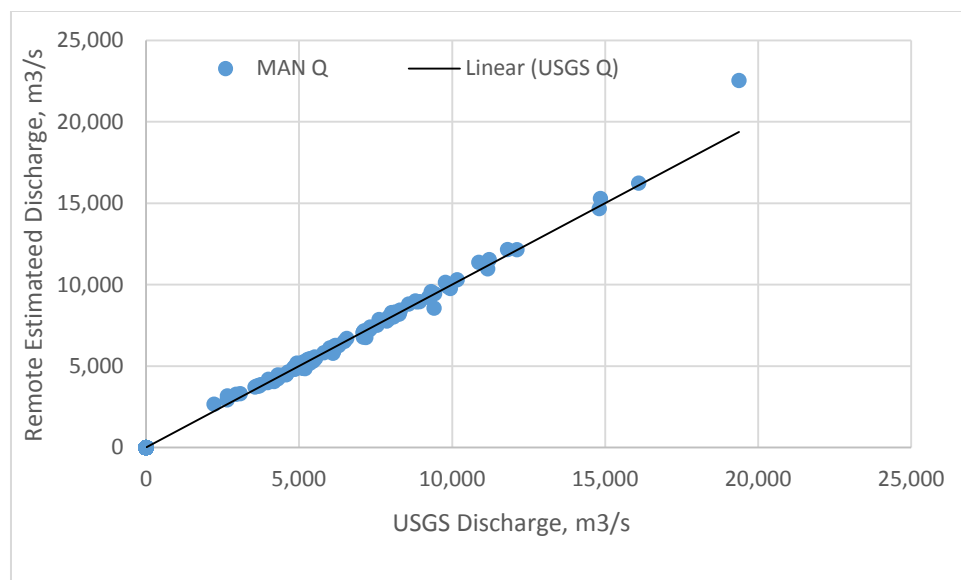
Figure 14 – Jason-2 observed water surface slope variation over time for the Yukon River reach near Stevens Village, Alaska.



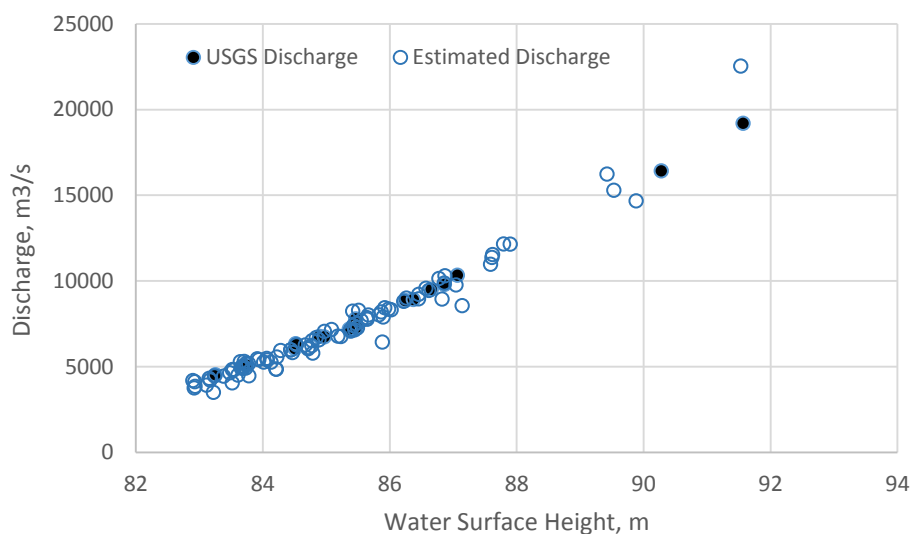
A



B

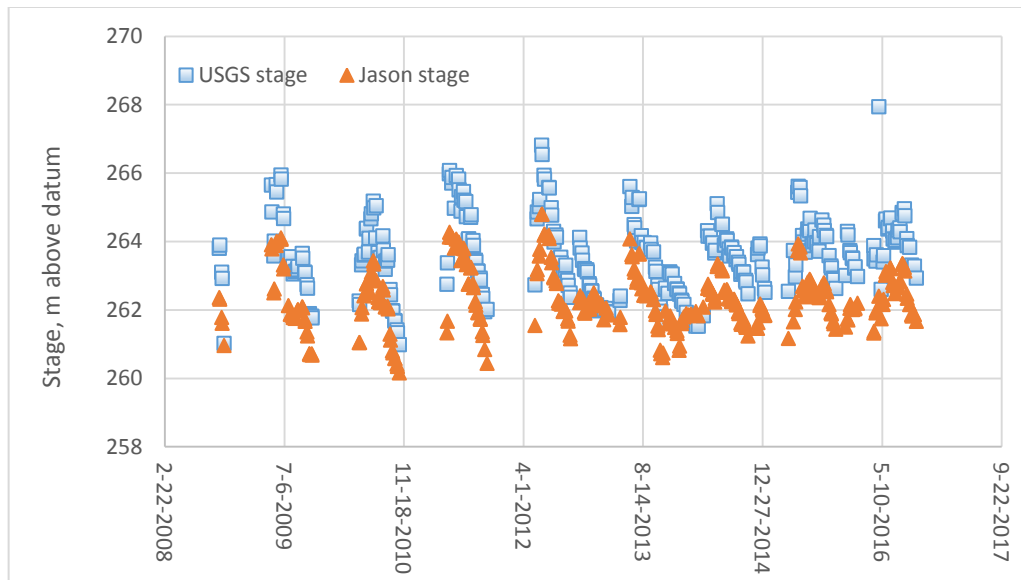


C

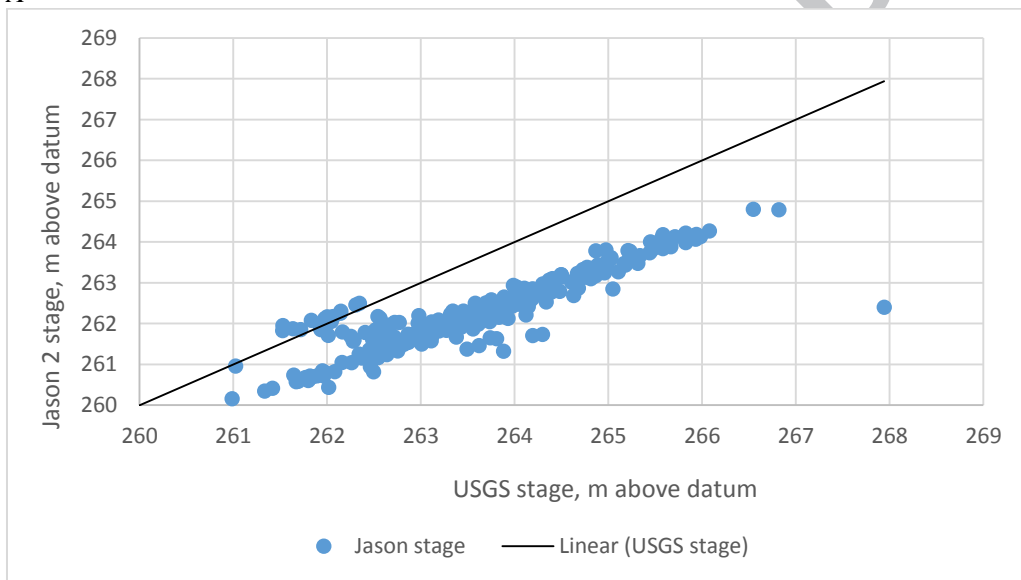


D

Figure 15 – Estimated uncalibrated river discharge using the MAN and the PVK equations (A and B) compared to the USGS measured discharge for the Yukon River reach near Stevens Village, Alaska; the calibrated estimated discharge versus USGS discharge for the MAN equation (C) and the calibrated stage-discharge relation for the estimated discharge compared to the USGS measured stage-discharge relation (D).



A



B

Figure 16 – Average Jason-2 (average of upstream and downstream) and USGS river heights for the Yukon River reach at Eagle, Alaska, over the 8 year period (A) and (B) showing the linear one-to-one line.



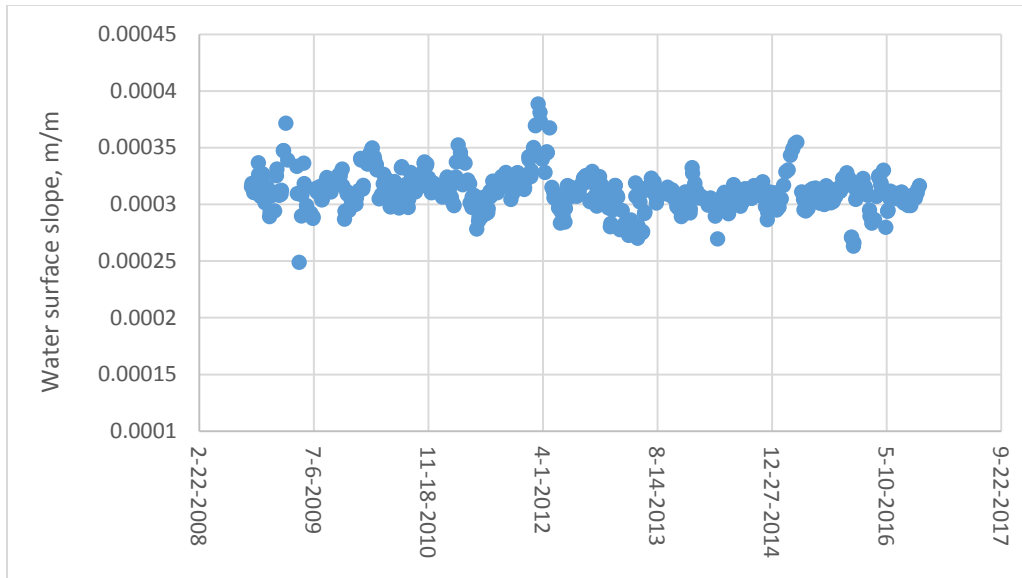
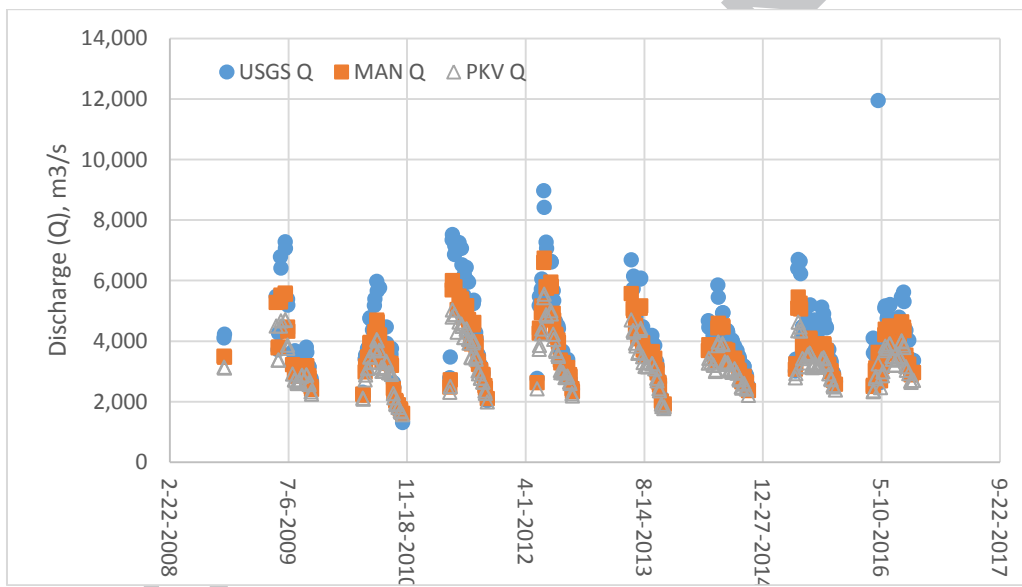
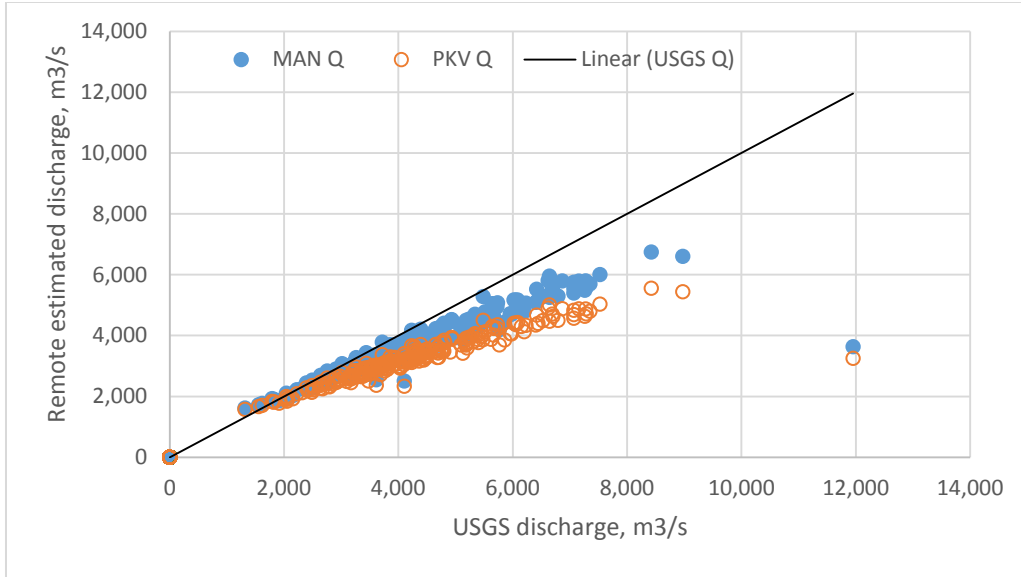


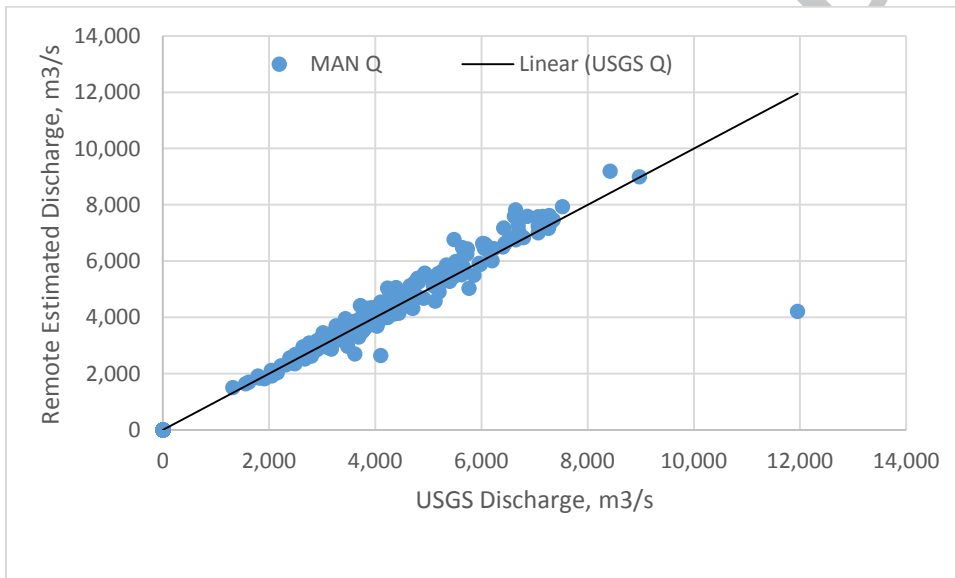
Figure 17 – Jason-2 observed water surface slope variation over time for the Yukon River reach at Eagle, Alaska.



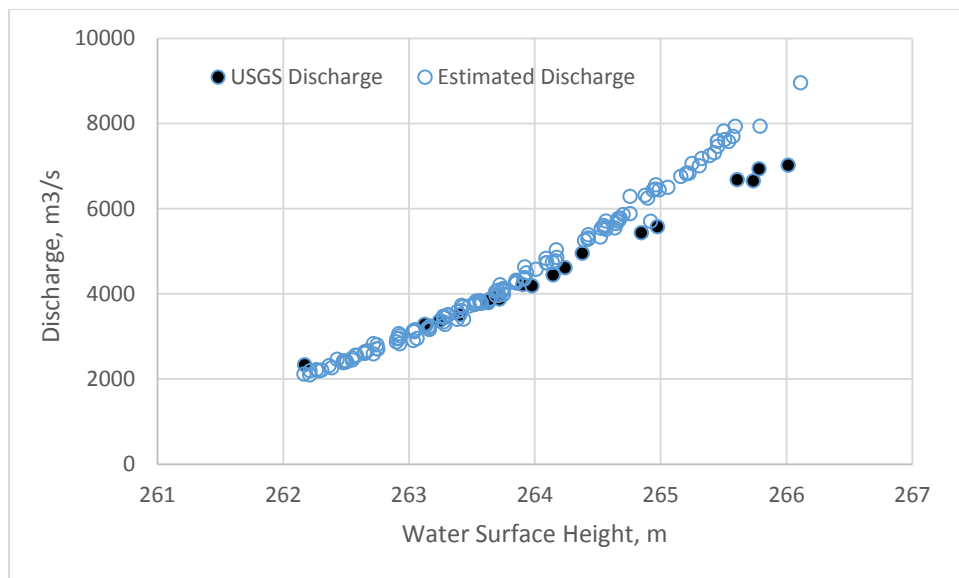
A



B



C



D

Figure 18 – Estimated uncalibrated river discharge using the MAN and the PVK equations (A and B) compared to the USGS measured discharge for the Yukon River reach at Eagle, Alaska; the calibrated estimated discharge versus USGS discharge for the MAN equation (C) and the calibrated stage-discharge relation for the estimated discharge compared to the USGS measured stage-discharge relation (D).

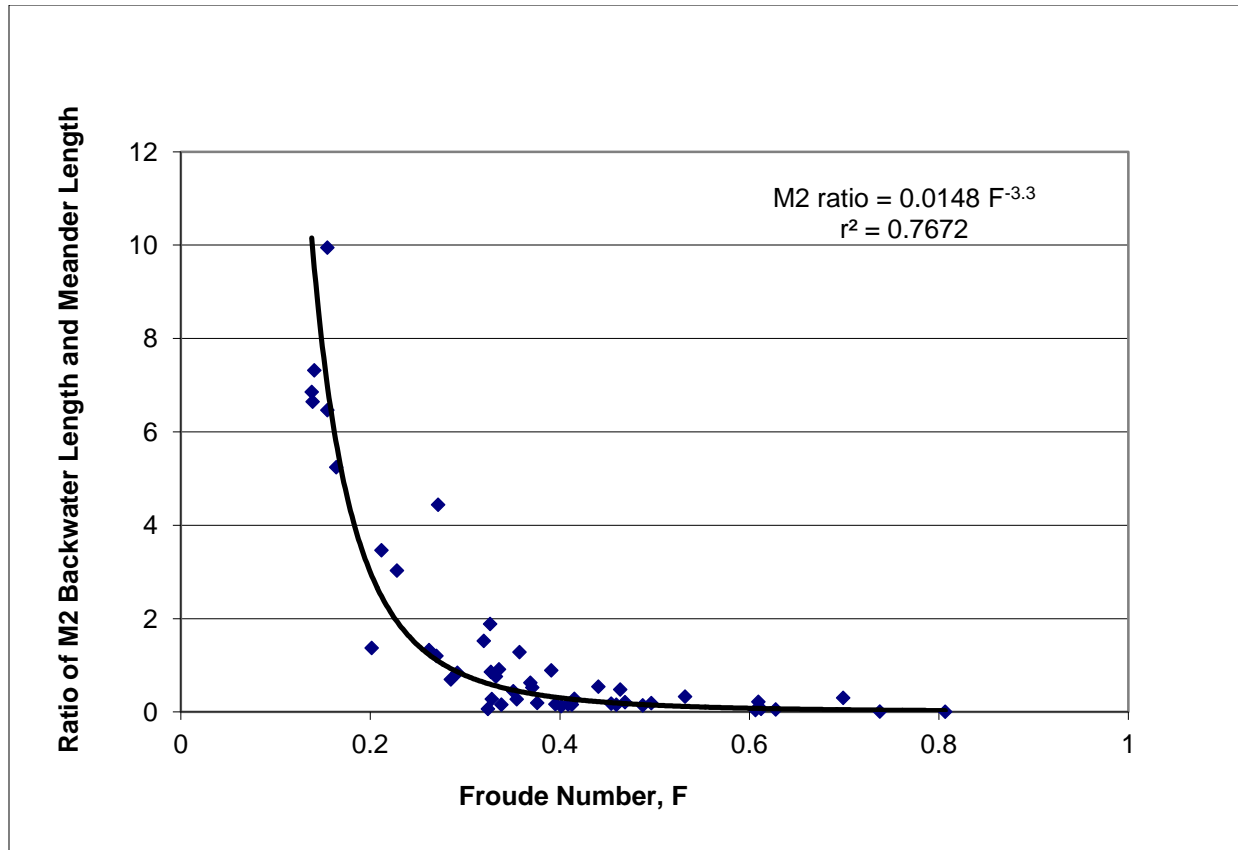


Figure 19 - Ratio of backwater to resistance length as a function of Froude number for natural rivers, showing the logarithmic best fit line given by the equation shown on the chart with the associated coefficient of determination ( $r^2$ ).

**Table 1 - Hydraulic Variables Necessary for Estimating Discharge**

**Basic Methods**

|  |   |
|--|---|
| $Q = W * Y * V$  | $Q =$ discharge, $Y =$ mean flow depth, $V =$ mean flow velocity, $W =$ water surface width |
| Manning<br>$V = Y^{0.67} S^{0.5} / n$                        | $S =$ water surface slope, $n =$ Manning roughness coefficient                              |
| Prandtl-von Karman<br>$V = 2.5 (gYS)^{0.5} (\ln(Y/y_0) - 1)$ | $g =$ gravitational constant, $y_0 =$ roughness height                                      |
| $Y = (Stage - B) * (1 - (1/1+b))$                            | $B =$ channel bottom height, $b =$ shape factor   |

**Observed Variables**

|                |  |
|----------------|--|
| W              | Average water surface width in reach - Measured from Landsat     |
| Stage          | Water surface Height - Measured from Jason-2 satellite altimeter |
| Slope          | Water surface slope - Measured from Jason-2 satellite altimeter  |
| Meander Length | River channel meander length - Measured from Landsat             |

**Derived Variables**

|       |   |
|-------|---|
| B     | River channel bottom elevation - estimated from relation between stage and W    |
| $V_b$ | Bankfull reference mean flow velocity - estimated from slope and meander length |

|       |   |
|-------|---|
| $Y_b$ | Bankfull reference mean depth of flow - estimated from $V_b$ and slope                        |
| $n$   | Manning roughness coefficient - estimated from depth and bankfull Manning roughness ( $n_b$ ) |
| $n_b$ | Bankfull reference Manning roughness coefficient - estimated from slope, $V_b$ , and $Y_b$    |
| $r$   | Channel shape coefficient - assumed as a constant value of 2                                  |
| $Y_0$ | Prandtl-von Karman roughness height - estimated from $Y_b$ and $n_b$                          |

Table 2 – Jason-2 and ICESat comparative observations

| Satellite Pass       | Pass Location lat/lon(deg) | Overpass Channel Width (Approx, m) | Pass-Pair Thalweg (km) | Pass-Pair Time Diff. (days) | Reach Slope |
|----------------------|----------------------------|------------------------------------|------------------------|-----------------------------|-------------|
| <b>EAGLE REACH</b>   |                            |                                    |                        |                             |             |
| <i>Jason-2</i>       |                            |                                    |                        |                             |             |
| Pass251              | 64.639/-140.887            | 850                                | 34.5                   | 2                           | 0.000312*   |
| Pass204              | 64.844/-141.135            | 700                                |                        |                             |             |
| <i>ICESat</i>        |                            |                                    |                        |                             |             |
| Pass0289(2)          | 64.735/-141.041            | 1450                               | 76.6                   | 7-8                         | 0.000275**  |
| Pass0178             | 65.120/-141.645            | 1335                               |                        |                             |             |
| Pass0289(1)          | 64.686/-141.020            | 640                                | 76.8                   | 41                          | 0.000291    |
| Pass0044             | 65.112/-141.525            | 1555                               |                        |                             |             |
| Pass0297(1)          | 64.698/-141.040            | 980                                | 81.3                   | 8                           | 0.000273    |
| Pass0178             | 65.120/-141.645            | 1335                               |                        |                             |             |
| Pass0289(1)          | 64.686/-141.020            | 640                                | 83.2                   | 8                           | 0.000267    |
| Pass0178             | 65.120/-141.645            | 1335                               |                        |                             |             |
| Pass1279(1)          | 64.540/-140.581            | 2310                               | 117.0                  | 16                          | 0.000301    |
| Pass0044             | 65.112/-141.525            | 1555                               |                        |                             |             |
| Pass1279(1)          | 64.540/-140.581            | 2310                               | 122.3                  | 17                          | 0.000295    |
| Pass0178             | 65.120/-141.645            | 1335                               |                        |                             |             |
| Pass1279(2)          | 64.518/-140.589            | 750                                | 126.8                  | 17                          | 0.000325    |
| Pass0178             | 65.120/-141.645            | 1335                               |                        |                             |             |
| <b>STEVENS REACH</b> |                            |                                    |                        |                             |             |
| <i>Jason-2</i>       |                            |                                    |                        |                             |             |
| Pass227(1)           | 65.865/-149.289            | 3195                               | 36.8                   | 0                           | 0.000091*** |
| Pass227(2)           | 65.819/-149.992            | 3083                               |                        |                             |             |
| <i>ICESat</i>        |                            |                                    |                        |                             |             |
| Pass0342(8)          | 65.939/-149.235            | 3240                               | 119.9                  | 0                           | 0.000104    |
| Pass0334(2)          | 65.508/-150.173            | 730                                |                        |                             |             |
| Pass0342(1)          | 65.944/-149.236            | 3240                               | 124.3                  | 8                           | 0.000104    |
| Pass0223(1)          | 65.491/-150.242            | 610                                |                        |                             |             |

Channel widths are approximate. Reach slopes are averages based on (\*) May to November 2008-2016, (\*\*) March, April and November 2006-2008, and (\*\*\*) May to October 2008-2016 measurements.

Table 3 – Landsat Image Analysis Data for the Yukon River Stevens Village Reach

| Landsat Image | Average Reach | Average Jason- | USGS stage m |
|---------------|---------------|----------------|--------------|
|---------------|---------------|----------------|--------------|

| Date      | Width | 2_stage |      |
|-----------|-------|---------|------|
|           | m     | m       |      |
| 9/19/2010 | 627.5 | 83.1    | 83.6 |
| 9/28/2010 | 592.2 | 82.4    | 82.4 |
| 5/30/2010 | 610.8 | 83.4    | 84.2 |
| 6/18/2011 | 659.3 | 85.2    | 85.3 |

Table 4 – Landsat Image Analysis Data for the Yukon River Eagle Reach

| Landsat Image Date | Average Reach Width | Average Jason-2_stage | USGS stage m |
|--------------------|---------------------|-----------------------|--------------|
|                    | m                   | m                     |              |
| 9/5/2011           | 535.5               | 262.6                 | 263.9        |
| 8/29/2011          | 545.4               | 263                   | 264.6        |
| 9/12/2011          | 513.9               | 262.3                 | 263.5        |
| 5/25/2011          | 548.3               | 263.5                 | 265.8        |

**Table 5 - Stage Statistics Stevens Village**

Stdev = Standard deviation; Max = maximum; Min = Minimum

| Stage                             | USGS m | Jason stage m | Difference m |
|-----------------------------------|--------|---------------|--------------|
| Mean                              | 84.10  | 83.72         | -0.38        |
| Stdev                             | 2.30   | 2.32          | 0.25         |
| Max                               | 91.62  | 91.15         | 0.75         |
| Min                               | 80.33  | 79.86         | -1.11        |
| Nash-Sutcliffe Efficiency         |        |               | 0.96         |
| Normalized Root Mean Square Error |        |               | 0.04         |

**Table 6 - Discharge Statistics Stevens Village**

Stdev = Standard deviation; CV = coefficient of variation; Max = maximum; Min = Minimum

| Uncalibrated Discharge            | USGS     | MAN      | PKV      | Error MAN percent | Error PKV percent | Error Man log | Error PKV log |
|-----------------------------------|----------|----------|----------|-------------------|-------------------|---------------|---------------|
| Mean                              | 6975.33  | 7660.69  | 7177.59  | 0.13              | 0.08              | 0.05          | 0.03          |
| Stdev                             | 3036.42  | 2934.24  | 2294.83  | 0.10              | 0.15              | 0.04          | 0.06          |
| CV                                | 0.44     | 0.38     | 0.32     |                   |                   |               |               |
| Max                               | 19370.90 | 21293.75 | 17241.06 |                   |                   |               |               |
| Min                               | 2221.09  | 3431.28  | 3664.47  |                   |                   |               |               |
|                                   |          |          |          | MAN               | PKV               |               |               |
| Nash-Sutcliffe Efficiency         |          |          |          | 0.94              | 0.93              |               |               |
| Normalized Root Mean Square Error |          |          |          | 0.04              | 0.05              |               |               |

| Calibrated to 3 Measurements      |          |          | Error          |
|-----------------------------------|----------|----------|----------------|
| Discharge                         | USGS     | MAN      | MAN<br>percent |
| Mean                              | 6975.33  | 7047.00  | 0.01           |
| Stdev                             | 3036.42  | 3202.90  | 0.05           |
| Coef.                             |          |          |                |
| Var.                              | 0.44     | 0.45     |                |
| Max                               | 19370.90 | 22534.75 |                |
| Min                               | 2221.09  | 2663.53  |                |
|                                   |          |          | MAN            |
| Nash-Sutcliffe Efficiency         |          |          | 0.98           |
| Normalized Root Mean Square Error |          |          | 0.02           |

**Table 7 - Stage statistics Eagle**

Stdev = Standard deviation; Max = maximum; Min = Minimum

| Stage                             | USGS<br>m | Jason stage<br>m | Difference<br>m |
|-----------------------------------|-----------|------------------|-----------------|
| Mean                              | 263.64    | 262.33           | -1.32           |
| Stdev                             | 1.12      | 0.85             | 0.52            |
| Max                               | 267.94    | 264.80           | 0.43            |
| Min                               | 260.99    | 260.16           | -5.54           |
| Nash-Sutcliffe Efficiency         |           |                  | -0.61           |
| Normalized Root Mean Square Error |           |                  | 0.20            |

**Table 8 - Discharge Statistics Eagle**

Stdev = Standard deviation; CV = coefficient of variation; Max = maximum; Min = Minimum

| Uncalibrated              |          |         |         | Error          | Error          | Error      | Error      |
|---------------------------|----------|---------|---------|----------------|----------------|------------|------------|
| Discharge                 | USGS     | MAN     | PKV     | MAN<br>percent | PKV<br>percent | Man<br>log | PKV<br>log |
| Mean                      | 4273.79  | 3682.54 | 3263.02 | -0.12          | -0.21          | -0.06      | -0.11      |
| Stdev                     | 1427.48  | 978.10  | 763.40  | 0.08           | 0.09           | 0.05       | 0.05       |
| Coef.                     |          |         |         |                |                |            |            |
| Var.                      | 0.33     | 0.27    | 0.23    |                |                |            |            |
| Max                       | 11952.15 | 6745.70 | 5555.14 |                |                |            |            |
| Min                       | 1316.01  | 1618.35 | 1574.28 |                |                |            |            |
|                           |          |         |         | MAN            | PKV            |            |            |
| Nash-Sutcliffe Efficiency |          |         |         | 0.62           | 0.19           |            |            |

|                                   |      |      |
|-----------------------------------|------|------|
| Normalized Root Mean Square Error | 0.08 | 0.12 |
|-----------------------------------|------|------|

| Calibrated to 3 Measurements      |          |         | Error<br>MAN<br>percent |
|-----------------------------------|----------|---------|-------------------------|
| Discharge                         | USGS     | MAN     |                         |
| Mean                              | 4273.79  | 4364.25 | 0.02                    |
| Stdev                             | 1427.48  | 1457.91 | 0.08                    |
| Coef.                             |          |         |                         |
| Var.                              | 0.33     | 0.33    |                         |
| Max                               | 11952.15 | 9196.48 |                         |
| Min                               | 1316.01  | 1507.01 |                         |
| Nash-Sutcliffe Efficiency         |          |         | 0.83                    |
| Normalized Root Mean Square Error |          |         | 0.06                    |

#### Highlights

Jason-2 altimetry observed water surface height and slope dynamics Yukon River Alaska

The USGS Dynamic Surface Water Extent applied to Landsat estimated the mean width

The remote observations were used to estimate the river depth, velocity, and discharge

The remotely sensed discharge was estimated within 5% of measured USGS discharge

Historical time series of discharge could be developed from archived information